

BRNO UNIVERSITY OF TECHNOLOGY

VYSOKÉ UČENÍ TECHNICKÉ V BRNĚ

FACULTY OF MECHANICAL ENGINEERING

FAKULTA STROJNÍHO INŽENÝRSTVÍ

INSTITUTE OF SOLID MECHANICS, MECHATRONICS AND BIOMECHANICS

ÚSTAV MECHANIKY TĚLES, MECHATRONIKY A BIOMECHANIKY

THE NUMERICAL ANALYSIS OF INTERACTIONS BETWEEN TWINS AND PRECIPITATES IN MAGNESIUM ALLOYS

NUMERICKÁ ANALÝZA INTERAKCE DVOJČAT S PRECIPITÁTY V HOŘČÍKOVÝCH SLITINÁCH

MASTER'S THESIS

DIPLOMOVÁ PRÁCE

AUTHOR

AUTOR PRÁCE

Bc. Miloš Bogdan

SUPERVISOR

VEDOUCÍ PRÁCE

Dr. Ing. Filip Šiška, Ph.D.

BRNO 2017

Zadání diplomové práce

Ústav:	Ústav mechaniky těles, mechatroniky a biomechaniky
Student:	Bc. Miloš Bogdan
Studijní program:	Aplikované vědy v inženýrství
Studijní obor:	Inženýrská mechanika a biomechanika
Vedoucí práce:	Dr. Ing. Filip Šiška, Ph.D.
Akademický rok:	2016/17

Ředitel ústavu Vám v souladu se zákonem č.111/1998 o vysokých školách a se Studijním a zkušebním řádem VUT v Brně určuje následující téma diplomové práce:

Numerická analýza interakce dvojčat s precipitáty v hořčíkových slitinách

Stručná charakteristika problematiky úkolu:

Práce se bude zabývat numerickou analýzou napěťových polí indukovaných deformačním dvojčatěním a jejich změnami v důsledku přítomnosti precipitátů. Analýza bude založena na 2D a 3D simulacích metodou konečných prvků s využitím teorie krystalové plasticity.

Cíle diplomové práce:

1. Vytvoření 2D FEM modelu dvojčete v matici obsahující precipitáty.
2. Analýza indukovaných polí v závislosti na velikosti a rozložení precipitátů při různých hodnotách kritických skluzových napětí.
3. Návrh a diskuze mechanismů interakce a jejich vlivu na růst dvojčat.

Seznam doporučené literatury:

SISKA, F. et al., Numerical analysis of twin thickening process in magnesium alloys, Acta Materialia 124, 2017

ROBSON, J.: The effect of internal stresses due to precipitates on twin growth in magnesium, Acta Materialia 121, 2016

BARNETT, M. R. et al., Plastic relaxation of the internal stress induced by twinning, Acta Materialia 61, 2013

KUMAR, M. A. et al., Effect of local stress fields on twin characteristics in HCP metals, Acta Materialia 116, 2016

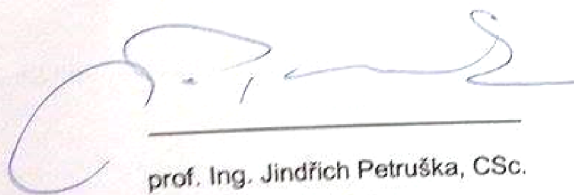
KUMAR, M. A. et al., Numerical study of the stress state of a deformation twin in magnesium, Acta Materialia 84, 2015

CHRISTIAN, J. W. et al., Deformation twinning, Progress in Materials Science 39. 1995

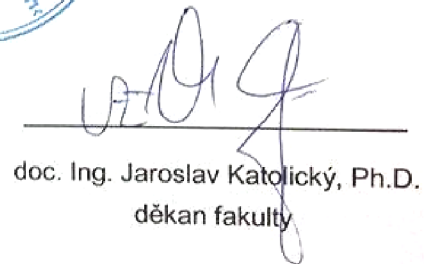
Fakulta strojního inženýrství, Vysoké učení technické v Brně / Technická 2896/2 / 616 69 / Brno

Termín odevzdání diplomové práce je stanoven časovým plánem akademického roku 2016/17

V Brně, dne 9. 12. 2016



prof. Ing. Jindřich Petruška, CSc.
ředitel ústavu



doc. Ing. Jaroslav Katolický, Ph.D.
děkan fakulty

ABSTRAKT

Hlavním cílem této práce je analýza napěťových polí, indukovaných dvojčatěním ovlivněných přítomností precipitátů před čelem dvojčete. Zvolený případ popisuje tahové dvojče $\{1012\} \langle 10\bar{1}1 \rangle$ s lamelárními precipitáty v hořčíkové slitině AZ31. Systém je modelován metodou konečných prvků jako 2D elastická eliptická inkluze, se dvěma elastickými precipitáty tyčovitěho tvaru, nacházející se před čelem elipsy obklopené plastickou maticí modelovanou pomocí krystalové plasticity. Analýza dvojčat a precipitátů s různou tloušťkou ukazuje inhibující účinek precipitátů na růst tloušťky dvojčat. Velikost tohoto účinku se mění s tloušťkou dvojčete v důsledku komplexní interakce mezi dvojčetem precipitátem a indukovanou plastickou zónou.

Klíčová slova

Hořčíkové slitiny, Dvojčatění, Precipitáty, MKP, Krystalová plasticita

ABSTRACT

The main objective of this thesis is to analyse the stress fields induced by twinning and their alteration due to the presence of precipitates at the twin tips. Analysed case describes $\{1012\} \langle 10\bar{1}1 \rangle$ tensile twin with lamellar precipitates in magnesium alloy AZ31. The system is modelled using FE method as the 2D elastic elliptical inclusion with two rod like elastic precipitates in front of the ellipse embedded in plastic matrix modelled using crystal plasticity theory. Analysis of twins and precipitates with different thickness shows the inhibitory effect of precipitates on twin thickening. An intensity of this effect is changing with the twin thickness due to the complex interaction between twin, precipitate and induced plastic zone.

Key words

Magnesium alloys, Twinning, Precipitates, FEM, Crystal plasticity

BIBLIOGRAFICKÁ CITACE

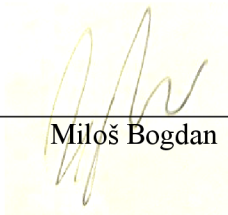
BOGDAN, M. Numerická analýza interakce dvojčat s precipitáty v hořčíkových slitinách. Brno: Vysoké učení technické v Brně, Fakulta strojního inženýrství, 2017. 60 s. Vedoucí diplomové práce Dr. Ing. Filip Šiška, Ph.D..

PROHLÁŠENÍ

Prohlašuji, že jsem diplomovou práci na téma **Numerická analýza interakce dvojčat s precipitáty v hořčkových slitinách** vypracoval samostatně s použitím pramenů, uvedených na seznamu, který tvoří přílohu této práce.

25. 5. 2017

V Brně dne



Miloš Bogdan

PODĚKOVÁNÍ

Děkuji tímto Dr. Ing. Filipu Šiškoví, Ph.D. za odborné vedení při psaní této práce, cenné připomínky, rady a studijní materiály. V neposlední řadě bych mu také chtěl poděkovat za trpělivost a vstřícný přístup. Dále bych chtěl poděkovat svým rodičům, přítelkyni a všem dalším, kteří mi jakkoliv pomohli a podporovali mě.

CONTENTS

1. Introduction	10
2. Magnesium	11
2.1. Occurrence and extraction	11
2.2. Characteristic properties	12
2.3. Magnesium alloys	12
2.3.1. Alloying elements	13
2.3.2. Alloys identification	14
2.3.3. Classification	15
2.3.3.1. Alloys for casting	15
2.3.3.2. Alloys for wrought parts	16
2.3.4. Alloys applications	18
3. Deformation mechanisms in magnesium	19
3.1. Hexagonal close packed crystallographic structure	19
3.1.1. Miller – Bravais system	19
3.2. Deformation mechanisms	20
3.2.1. Deformation by slip	21
3.2.2. Deformation by twinning	26
4. Finite element method	29
4.1. The stress – strain analysis by FEM	29
4.1.1. Mesh and elements	29
4.1.2. Loads and boundary conditions	30
4.1.3. Strain definition	30
4.1.4. The equilibrium law	30
4.1.5. The constitutive equations	31
4.1.6. FEM solution methods for elastic material	31
5. Objectives	34
6. Numerical model definition	35
6.1. Topology and geometry of the twin and precipitates	35
6.2. Model of the geometry	35
6.3. Boundary conditions and loading	36
6.4. The material model	37
6.4.1. The material model based on the crystal plasticity theory	37
6.4.2. Input data	38

7. Results	40
7.1. Mesh convergence	40
7.1.1. Model setting.....	40
7.1.2. Element size influence on X'Y' shear stress and strain	41
7.1.3. Validation of the numerical model.....	43
7.1.4. Mesh density setting.....	44
7.2. Numerical analysis of the twin and precipitate interaction	46
7.2.1. Twin average results.....	46
7.2.2. Twin boundary results	49
8. Discussion.....	52
9. Conclusions	55
10. References	56
11. Used symbols and variables.....	59

1. Introduction

Currently, high-technology companies increasingly rely on the technical and economic potential of innovative materials. Additionally, politics and public are demanding a more economical and ecological use of primary energy sources, in order to reduce carbon emissions and lower the growing environmental impact. For industry branches, such as automotive or aerospace industry, use of light metals as construction materials on account of fuel efficiency of their products is becoming of key importance. Magnesium seems to fulfill the demands for low weight materials perfectly as it is the lightest of all metals. It is also fairly strong and has good damping properties. Its excellent machinability, good recycling potential and worldwide availability make it even more industrially interesting [1]. These could be the main reasons why the interest in magnesium alloys increased excessively over past several years.

Magnesium was discovered by the British chemist Sir Humphrey Davy in 1808 and isolated by the French chemist H. Bussy in 1828. The history of magnesium from a curiosity metal to an industrial material was greatly affected by wars. Back then, the driving force behind the development of magnesium alloys was the potential for lightweight construction in military applications. After World War II magnesium alloy use and development ceased while aluminium alloys and plastics were the main objects of interest among the lightweight materials [2].

Use of magnesium alloys has always been limited by economic and environmental limitations (extraction of pure magnesium is expensive and uses lots of energy). That is why production of magnesium alloys is insignificant compared to production of steel and aluminium alloys [3]. However present extraction methods keep getting improved and new methods are proposed, which could mean that more magnesium will be produced and used in future.

Even though magnesium alloys development and research have been running for several decades, there are still some unknowns that need to be revealed. For example, because of its hexagonal close packed (HCP) crystal structure, all the deformation processes and their impact on behaviour are not yet completely understood. In these materials, plastic deformation is carried out not only by slip, but deformation twinning plays a significant role too. An evolution of twinning is caused by an insufficient number of slip systems in crystal lattice. All the factors, which could affect twin growth and thus plastic deformation were not yet completely explored. In this thesis, interaction mechanisms between twin and precipitates in a single crystal with hexagonal close packed structure will be investigated via finite element simulations. A better understanding of the deformation processes could improve the use of magnesium in its current applications and eventually new applications [4].

2. Magnesium

Magnesium is a chemical element with symbol Mg and an atomic number of 12. It is an alkaline earth metal in Group II in the periodic table. In its pure and solid form (as shown in Figure 2.1) it is a silvery-white, shiny, light and relatively tough metal. Magnesium shows slight reactivity due to its electron configuration ($1s^2 2s^2 2p^6 3s^2$, its outer orbital is fully completed with two electrons, which magnesium tend to lose to form a cation with charge +2 and oxidation state +2). When burns, it produces bright, white light [7].



Figure 2.1 – Metal magnesium [5].

2.1. Occurrence and extraction

Due to its reactivity, magnesium naturally occurs only in combination with other elements. It can be found virtually everywhere as it is the fourth most common element in Earth (making up 13 % of planets mass). It is the third most abundant element dissolved in seawater and eight most abundant element in earth deposits. It is also commonly present in living creatures as it is essential for all the cells and majority of enzymes [7].

Industrially interesting resources are among the ore minerals, dolomite (a compound of magnesium and calcium carbonates, $MgCO_3 \cdot CaCO_3$), magnesite (magnesium carbonate, $MgCO_3$) and carnallite (a compound of magnesium and potassium chlorides and water, $MgCl_2 \cdot KCl \cdot 6H_2O$). Another resource is magnesium chloride ($MgCl_2$), which is dissolved in seawater and brines. In general, there are nowadays two principal extraction processes for the production of pure magnesium from natural resources: electrolysis and thermal reduction. Electrolysis can be used for extraction from almost all the natural resources. It consists of two steps: the preparation of a feedstock, containing anhydrous magnesium chloride, and the dissociation of this compound into magnesium metal and chlorine gas in electrolytic cells. The other, thermal reduction process is used for dolomite processing. Dolomite is calcinated to magnesium oxide (MgO) and lime (CaO) and magnesium oxide is then reduced by silicon or ferrosilicon. The final reaction is carried out at high temperatures, under very low pressure (close to vacuum). Under these conditions, the metal is produced as a vapour which is then condensed. Extracted magnesium needs to be purified and alloying elements are often added. Magnesium can be also recycled from old scrap metal [2,6,7].

2.2. Characteristic properties

Density	1738 kg/m ³
Youngs modulus	45 GPa
Ultimate tensile strength	80-180 Mpa
Fracture elongation	1-12 %
Melting point	650 °C
Boiling point	1090 °C

Table 2.1 – Physical and mechanical properties of magnesium.

Magnesium crystallizes at 650 °C in the hexagonal close packed structure. Below 225 °C, cold forming is impossible because from all deformation mechanisms mostly only {0001} <11 $\bar{2}$ 0> basal plane slip and {1012} <10 $\bar{1}$ 1> tensile twinning are active due to their low critical resolved shear stresses. That is why at room temperature, magnesium shows brittleness due to intercrystalline failure and local transcrystalline fracture at twin zones or basal planes. Above 225 °C {10 $\bar{1}$ 1} pyramidal planes slip is activated and magnesium shows good deformation behaviour. Among advantageous properties are the lowest density of all construction metals, high specific strength (strength/density ratio), good machinability, excellent casting behaviour (because of its great fluidity, even the most complicated die-cast parts can be produced, steel dies may be used), good damping properties (pure magnesium shows higher damping properties than cast-iron), good weldability under inert gasses and the possibility of integrated recycling. Along with the good properties, there are some disadvantages. As mentioned above, cold working is not possible. Pure magnesium is also very reactive and shows a high tendency for corrosion and creep at higher temperatures. Magnesium has a high degree of shrinkage, which leads to microporosity, low toughness and high notch sensitivity when cast [1].

2.3. Magnesium alloys

Pure magnesium metal is not usually used as the structural material because its negative properties mentioned above. However, an addition of alloying elements can reduce these negative effects and improve mechanical properties by the mechanisms of precipitation hardening and solid-solution hardening. While solid-solution hardening mainly depends on atomic radii of alloying elements, precipitation hardening is affected by a reduced solubility at low temperatures, the magnesium content of the intermetallic phase and its stability at application temperature. Magnesium forms intermetallic phases with most alloying elements. Stability of the phase increases with increasing electronegativity of the element [1].

2.3.1. Alloying elements

The most commonly used elements in magnesium alloys and their general effects on technological and mechanical properties are [1]:

- Silver improves tensile and creep properties at elevated temperatures in presence of rare earths but has a detrimental influence on corrosion behaviour.
- Aluminium is the most commonly used alloying element. It increases tensile strength and the hardness, although the hardness effect caused by the precipitated phase Mg₁₇Al₁₂ is only observable up to 120 °C. Besides these improvements, it also improves castability and has a minor influence on corrosion resistance. The disadvantage is a higher tendency for microporosity.
- Beryllium significantly reduces oxidation of melt surface at very low concentrations but leads to coarse grains.
Calcium has effective grain refining effect, causes slight suppression of oxidation of the molten metal and improves creep properties. On the other hand, it can lead to sticking to the tool during casting and to hot cracking. It also has a detrimental influence on corrosion behaviour.
- Copper, iron and nickel have a detrimental influence on corrosion behaviour and their limitation is necessary.
- Lithium increases evaporation and burning behaviour, so melting is only possible in protected and sealed furnaces. It is solid solution hardener at ambient temperatures, reduces density and enhances ductility. It strongly decreases corrosion properties, so coating to protect from humidity is necessary. Above 30 % Li-content, the lattice structure changes to FCC
- Manganese controls iron content by precipitating Fe-Mn compound. It is used for grain refinement, it increases creep resistance, improves corrosion behaviour due to iron control effect and also increases weldability.
- All rare earth elements (yttrium, neodymium, cerium) form the eutectic system of limited solubility with magnesium (precipitation hardening). Precipitates are very stable and improve elevated temperature tensile and creep properties as well as corrosion behaviour. These elements also improve castability and reduce microporosity.
- Silicon decreases castability, forms stable silicide compounds with many other alloying elements (compatible with Al, Zn, and Ag), improves creep properties and is a weak grain refiner. Its disadvantage is a detrimental influence on corrosion behaviour.
- Thorium is the most efficient alloying element. It suppresses microporosity, improves elevated temperature tensile and creep properties and improves ductility. However, because of its radioactivity, it has to be substituted by other elements.
- Zinc increases the fluidity of the melt and is a weak grain refiner, improves strength at ambient temperatures and its sufficient content compensates the detrimental effect of copper. It can also decrease shrinkage. As with aluminium, there is a tendency for microporosity and hot cracking.

- Addition of zirconium leads to an increase in tensile strength without a loss of ductility, because of its affinity for oxygen. The formed oxides are structure forming nuclei and aid grain refining. It is incompatible with Si, Al, and Mn and removes Fe, Al, and Si from the melt.

2.3.2. Alloys identification

The identification of magnesium alloys is standardized worldwide in the ASTM norm. Each alloy is marked with letters indicating the main alloying elements (code letters are shown in table 2.2), followed by rounded numbers, representing the elements in weight percent. The following section shows a degree of purity and is labelled by one letter (A to E) and the last section contains information about heat treatment. For example, the alloy AZ91E-T6 indicates magnesium alloy with 9 % Al and 1 % Zn, E means max. 0.005 % Fe, max. 0.0010% Ni and max. 0.015 % Cu, and T6 is solution heat treating and artificial aging [1].

Code letter	Allying element	Code letter	Allying element
A	Aluminium	M	Manganese
B	Bismuth	N	Nickel
C	Copper	P	Lead
D	Cadmium	Q	Silver
E	Rare Earth	R	Chromium
F	Iron	S	Silicon
G	Magnesium	T	Tin
H	Thorium	W	Yttrium
K	Zirconium	Y	Antimony
L	Lithium	Z	Zinc

Table 2.2 – ASTM code for designating magnesium alloys [1].

2.3.3. Classification

2.3.3.1. *Alloys for casting*

Casting is the dominant manufacturing process for magnesium components, representing about 98% of all its structural applications. The material can be cast by a variety of methods, including high-pressure diecasting, permanent mold casting, sand casting, semi-solid and squeeze casting. Different alloys may be specified for these different processes, but in cases where the same alloy is used with different casting processes, the properties of the finished castings will depend on the method. Die casting is the most widely used, because the excellent fluidity and filling characteristics of magnesium alloys allow large, thin-walled and complex castings to be economically produced by this process. Magnesium can be cast with thinner walls (1–1.5 mm) compared to aluminium (2–2.5 mm). This process also leads to fine-grained microstructure, better mechanical properties and lower microporosity compared to sand casting [1,8,10].

For castings, AZ91 is the most widely used magnesium alloy as it is less costly in comparison to other alloys and has good casting qualities and generally satisfactory resistance to corrosion. The corrosion resistance is impacted by the presence of impurities such as iron and nickel. In order to improve this property higher-purity versions of AZ91 are used. The aluminium in the alloy causes an increase in the tensile strength and hardness of the alloy to a temperature of 120 °C and improves castability. The disadvantage to this alloy is its susceptibility to creep at temperatures above 120 °C [9].

In applications where greater ductility and fracture toughness are required manganese is used instead of zinc, and aluminium content is lowered. Commercially used alloys are AM60, AM50 and AM20. If silicon is introduced into the Mg-Al alloys, creep properties can be improved. Two such alloys used in automotive applications are AS41 and AS21, while AS21 performs better with less aluminium and AS41 is easier to cast with better fluidity [9,10].

Another commonly used alloys are Mg-Zn-Zr alloys, namely ZK51 and ZK61 with 5 - 6 % Zinc and 1 % Zirconium. While previously mentioned Mg-Al alloys are mainly used for die-cast parts, Mg-Zn-Zr ones are mainly sand cast. These alloys possess good strength because zinc addition causes solution strengthening and zirconium leads to great grain refinement. On the other hand, these alloys are susceptible to microporosity and are not weldable [1,9,10].

In order to improve high temperature properties, rare earths are added. EZ33, QE22 and WE54 are some of the alloys containing rare earths used today. These alloys are highly heat, creep, corrosion and ageing resistant, have good fatigue strength, but are very expensive due to a cost of alloying elements [10].

An overview of the most commonly used cast alloys, their chemical composition, tensile mechanical properties, the technology of casting and applications are shown in Table 2.3 [1,8,9,10,12].

Alloy	Chemical composition	Tensile mechanical properties Rp0,2/Rm/A5 (MPa/MPa/%)	Characteristics and applications
AZ91	Mg-9Al-0,7Zn-0,3Mn	170/270/4,5	Die-cast, T6 treated, sand-castings are TIG weldable, most commonly used, applications: automotive, aerospace, bicycles, ladders, luggage, portable power tools, printing machinery and enclosures for electric devices
AM60	Mg-6Al-0,4Mn-0,2Zn	130/220/8	Die-cast, automotive components
AM50	Mg-5Al-0,4Mn-0,2Zn	125/210/10	
AM20	Mg-2Al-0,2Mn-0,2Zn	90/190/12	
AS41	Mg-4,2Al-0,35Mn-1Si	140/214/6	
ZK61	Mg-6Zn-0,8Zr	180/275/6	Sand cast, not weldable, applications where high strength is required
ZK51	Mg-4,6Zn-0,7Zr	138/234/5	
EZ33	Mg-2,6Zn-3,2RE-0,7Zr	96/138/5	Pressure tight sand or permanent mold cast, T5 treated
QE22	Mg-2,5Ag-2Nd-0,6Zr	175/240/2	Sand cast, T6 treated, weldable, advanced aerospace applications
WE54	Mg-5,25Y-3,5Nd-0,5Zr	170/250/2	

Table 2.3 – Most commonly used magnesium cast alloys overview.

2.3.3.2. Alloys for wrought parts

Because of the poor cold formability, magnesium alloys have to be worked at elevated temperatures (300 – 500 °C). Wrought alloys are typically produced in sheets, plates, extruded bars, shapes, tubes and forgings. High manufacturing costs have resulted in limited use of wrought alloys compared to cast alloys [11].

AZ31 is the most commonly used sheet and plate alloy and is the most widely used in applications at (or slightly above) room temperature. The strongest alloy for extrusion is AZ81, but the most common general purpose extruded alloy is AZ61. Magnesium forgings can only be fabricated from alloys with fine grained microstructures. Forgings are made

from AZ80 and ZK60 for parts that are to be used at ambient temperatures and WE43 is used for forging parts used at elevated temperatures. Forgings are important for manufacturing parts that have an intricate shape and must have strength higher than can be achieved by castings. Wrought magnesium components could be ideal for applications with a high demand for security or dynamic strength (automotive crash-relevant components), because of hot extrusion and forging (no pores or cavities and ideal microstructure due to thermomechanical treatment) but the cost inhibits the ability for wide use. Wrought alloys are under excessive development as well as working processes (the main goal is to reduce cost). Main applications of wrought magnesium components are in automotive industry, aeronautics and machinery. Overview of most commonly used alloys is shown in Table 2.4 and tensile mechanical properties of already used and developed alloys are shown in Figure 2.2 [9,10,11].

Alloy	Chemical composition	Tensile mechanical properties (Rp0,2/Rm/A5) (MPa/MPa/%)	Characteristics
M2	Mg-2Mn	160/215/4	Extrusion alloy for high performance with good weldability and corrosion resistance
AZ31	Mg-3Al-1Zn	160/240/10	
AZ61	Mg-6Al-2Zn	190/270/9	Extrusion and forging alloy with good strength and ductility, higher purity state to achieve better corrosion resistance
AZ80	Mg-8Al-0,5Zn	215/300/8	
ZK30	Mg-3Zn-0,6Zr	215/300/9	Excellent forging ability
ZK60	Mg-6Zn-0,6Zr	235/315/8	
WE43	Mg-4Y-3RE-0,5Zr	160/260/6	Extrusion and forging alloy with good high temperature strength
WE54	Mg-5,25Y-3,5RE-0,5Zr	180/280/6	

Table 2.4 – Most commonly used magnesium wrought alloys.

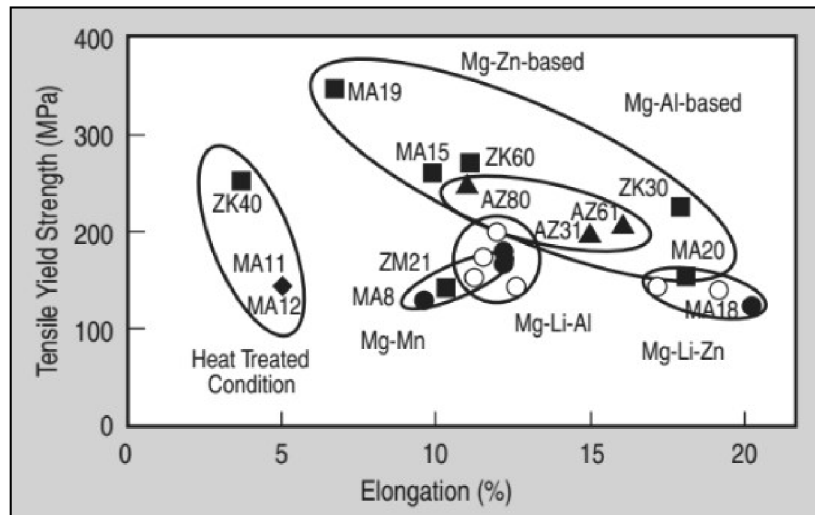


Figure 2.2 – The typical tensile strength and elongation for the most common commercial wrought magnesium alloys (solid symbols) and a number of experimental alloys (open symbols).

Note that these properties are dependent on the starting microstructure and processing conditions [11].

2.3.4. Alloys applications

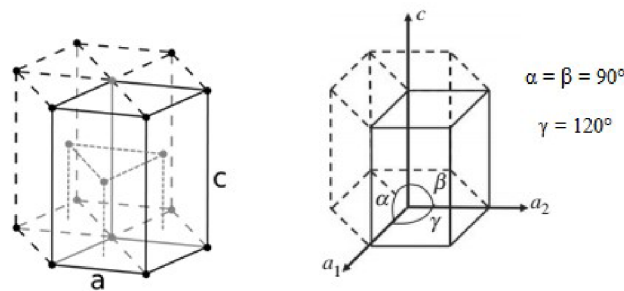
From around 1940 it was common to include magnesium cast parts in automobiles (crank case, camshaft sprocket, gearbox housing, several covers and other), until the change from air-cooled to water-cooled engines in around 1980. Other applications of cast alloys were gear boxes for helicopters, crank cases for zeppelin engines, air intake cases for propjet engines, frames, rims, etc.

The most common structural applications of magnesium today are aircraft and missile components (engine mounts, transmission cases, control hinges, fuel tanks, wings, seat frames), automotive components (wheel, housings, transmission cases, engine blocks, steering wheels, seat frames), bicycles, ladders, luggage, portable power tools (chainsaws, hedge clippers) and printing machinery. Because of its electromagnetic shielding properties and light weight is the metal also commonly used for enclosure of electric devices (laptops, televisions, cell phones, cameras). Magnesium alloys have also been used as a replacement for some engineering plastics due to their higher stiffness, good recycling capabilities and lower cost of production [7].

3. Deformation mechanisms in magnesium

3.1. Hexagonal close packed crystallographic structure

Magnesium has hexagonal close packed crystal structure. The cell of an HCP lattice can be visualized as a top and bottom plane of seven atoms, forming a hexagon around a central atom, and in between these planes is a formation of three atoms. There are two lattice parameters in HCP: a , and c , representing the basal and height parameter. HCP is the closest packing possible of spherical atoms, and for ideal HCP structure, c/a ratio is 1.633. Magnesium has c/a ratio of 1.624, but this value can be changed by some alloying elements [13,14,15].



Material	a (nm)	c (nm)	c/a
Magnesium	0.321	0.521	1.624

Figure 3.1 – Magnesium's HCP cell unit and lattice parameters [14].

3.1.1. Miller – Bravais system

Miller Bravais indices are used to specify planes and directions in the HCP structure giving four indices. These indices are based on four axes: three axes a_1 , a_2 , and a_3 , which are 120° apart in the basal plane, and the vertical c axis which is normal to the basal plane. Values of these indices are given by projections of the planes or directions onto the axes. The third index is the negative of the sum of the first two. Indices in round brackets (hkl) indicate single crystallographic planes, while indices in braces $\{hkl\}$ indicate a family of crystallographic planes that are equivalent to (hkl) by the symmetry of lattice. Similarly indices in square brackets $[hkl]$ indicate crystallographic direction, and indices in angle brackets $\langle hkl \rangle$ indicate a family of directions. Examples of planes and direction in HCP lattice, and their Miller-Bravais indices are shown in Figure 3.2 and 3.3 [16].

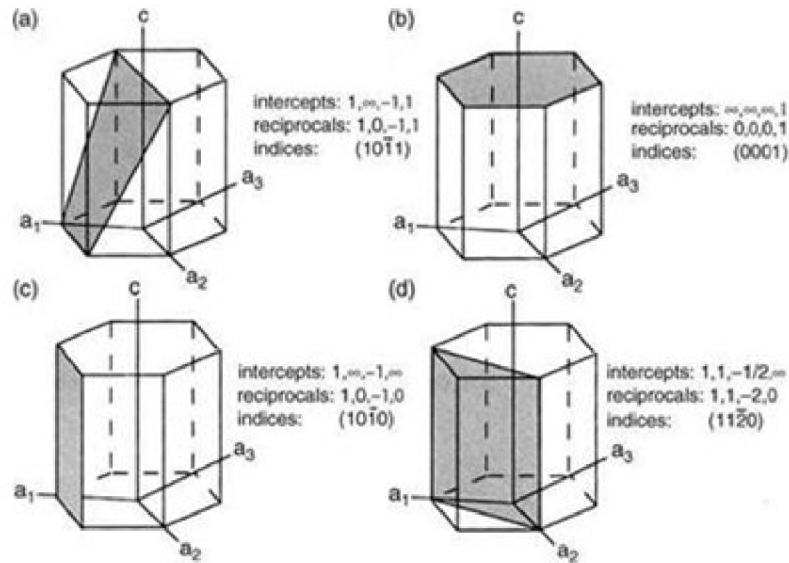


Figure 3.2 – Examples of HCP crystallographic planes and their Miller Bravais indices, (a) pyramidal plane, (b) basal plane, (c) prismatic plane, and (d) prismatic plane [16].

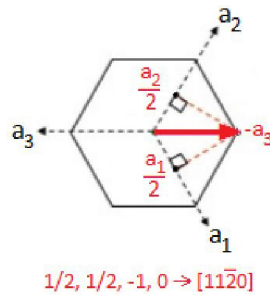


Figure 3.3 – Example of HCP crystallographic direction and its Miller Bravais indices, dashed red lines indicate projections onto a_1 and a_2 axes [17].

3.2. Deformation mechanisms

In general, there are two types of deformation of a crystalline material. Elastic deformation which is reversible, and plastic deformation which is irreversible. In unstrained crystalline solid, atoms are spaced at a distance, where their bonding energy is minimal (equilibrium separation). When the material is deformed within the elastic limit of the material, the distance between the atoms is changed, which leads to attraction or repulsion of the atoms, resulting in resistance of the material against the deformation (Figure 3.4). When the load is removed, atoms in the material return back into their original positions. This process is called elastic deformation. Because of the layout of the atoms in the crystal structure, almost all crystalline solids show elastic anisotropy at the single-crystal level. This means that the elastic properties of the material vary in different material directions [19,20].

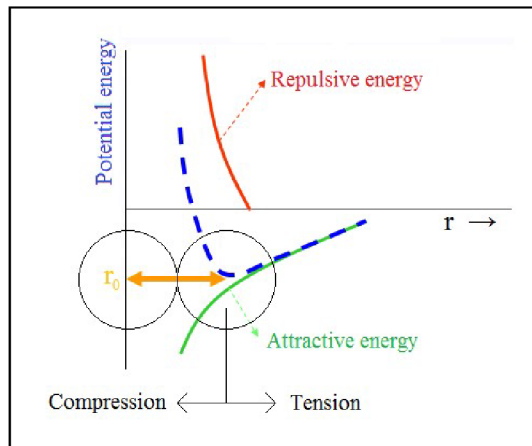


Figure 3.4 – Atomic bonding energy (r_0 – equilibrium separation) [19].

When the deformation exceeds the elastic limit of the material, atomic bonds split and reform. This process leads to permanent shape change, and is called plastic deformation. There are two prominent mechanisms of plastic deformation, namely slip and twinning [21].

3.2.1. Deformation by slip

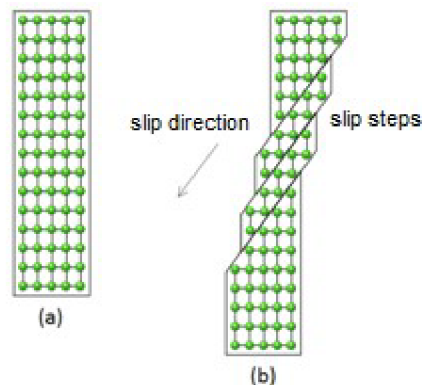


Figure 3.5 – Deformation by slip, (a) undeformed crystal, (b) after slip [21].

The micromechanism of slip is a cumulative motion of dislocations. Dislocations are linear crystal defects within a crystal structure. The main types of dislocations are: edge dislocation, screw dislocation, and mixed dislocation. Visualisation of the edge and screw dislocations and principles of their motion are shown in Figures 3.6 and 3.7. The dislocations are defined by the Burger's vector b which is a measure of the lattice distortion caused by the presence of an extra plane of atoms. The edge dislocation has the Burger's vector perpendicular to the dislocation line while the screw dislocation has it parallel to the dislocation line [20].

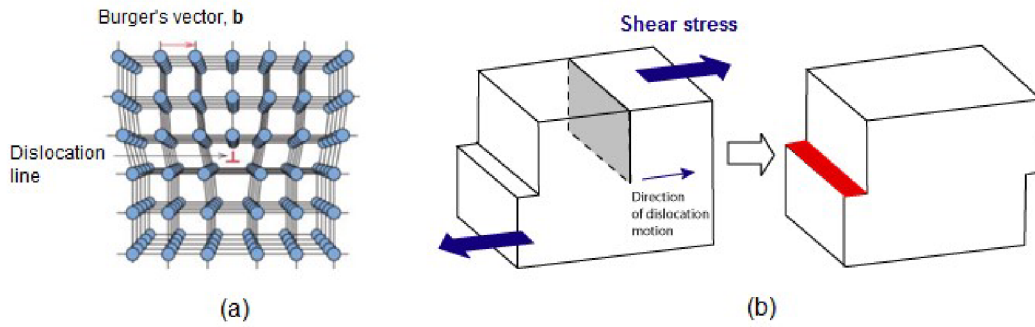


Figure 3.6 – (a) Scheme of an edge dislocation, (b) scheme of the edge dislocation motion [22,23].

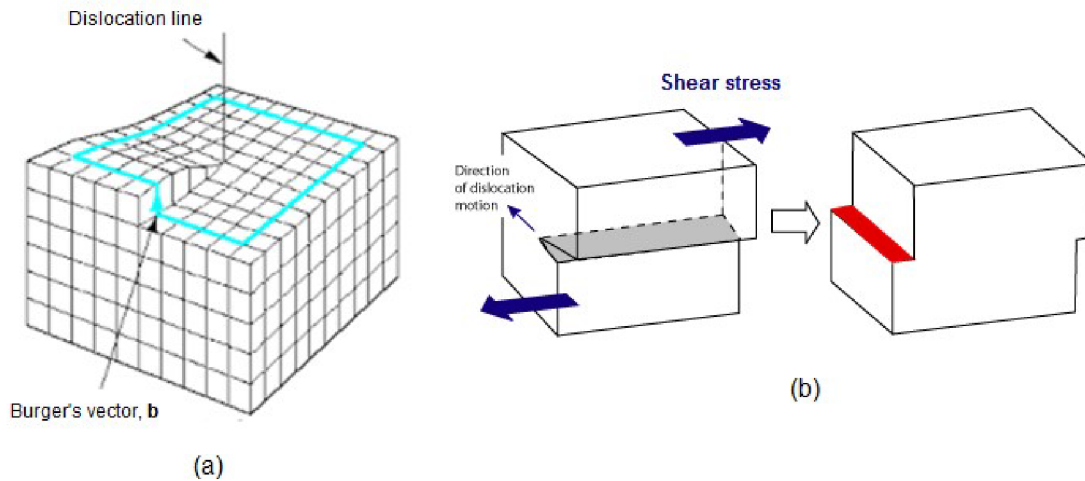


Figure 3.7 – (a) Scheme of a screw dislocation, (b) scheme of the screw dislocation motion [23, 24].

A shear stress τ acting on the slip plane and in the direction of the Burgers vector produces a force per unit length of dislocation that is perpendicular to the dislocation line and equal to τb . Dislocation starts to move, when the shear stress reaches a value called the critical resolved shear stress (CRSS). The strain energy per unit length of a dislocation in a crystal is:

$$W' = \alpha G b^2 \quad (3.1)$$

where α is a numerical factor between 0.5 and 1, and G is the shear modulus. Two parallel edge dislocations having the same slip plane have, when they are far apart, a combined energy equal to the sum of their individual energies, that is $2\alpha G b^2$ per unit length, since any interaction between them is negligible. When they are very close together and their Burgers vectors are equal and opposite, they will annihilate each other and the resulting energy will be zero, thus they attract each other in order to minimize the total energy. Like dislocations, on the other hand, when close together are equivalent to a single dislocation of Burgers vector $2b$, so that the energy per unit length is $\alpha G (2b)^2$, and therefore they repel each other in order to reduce the energy [20].

The number of dislocations typically present in an unstressed, annealed crystal is not sufficient to produce plastic strains greater than a few percent. In order to account for the large plastic strains that are actually produced, it is necessary for large numbers of dislocations to be created, and on a relatively small number of slip planes

in order to account for slip bands. The mechanisms for the multiplication of dislocations involve the Frank–Read source for the edge dislocations (Figure 3.8) and cross-slip and the Bardeen-Herring source for the screw dislocations [20].

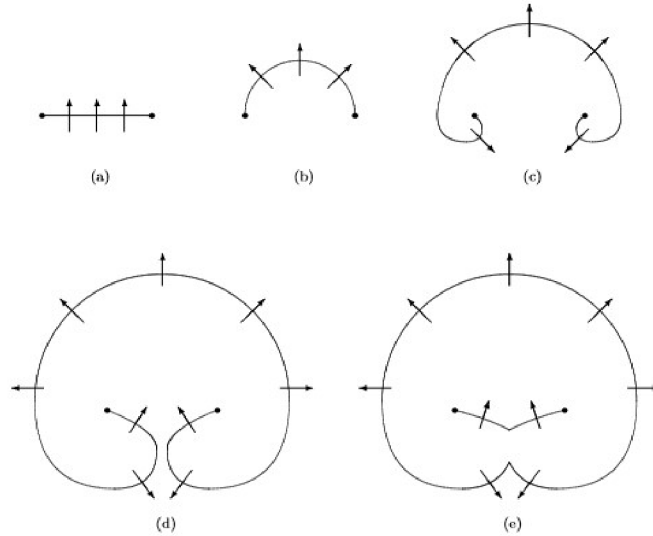


Figure 3.8 – The scheme of the Frank-Read source [20].

The Frank–Read source is a mechanism whereby a single segment of an edge dislocation, anchored at two interior points of its slip plane, can produce a large number of dislocation loops. The anchor points can be point defects, or points at which the dislocation joins other dislocations in unfavourable planes. If α in Equation is constant along the dislocation, independently of its orientation, then an increase ΔL in dislocation length requires an energy increment $W'\Delta L$, that is, work in that amount must be done on it. This is equivalent to assuming that a line tension T equal to W' is acting along the dislocation. In order to deform an initially straight dislocation segment into a circular arc subtending an angle 2θ , equilibrium requires a restoring force $F = 2T \sin\theta$ perpendicular to the original dislocation segment. If the length of the segment is L , then the force per unit length is F/L and can be produced by a shear stress $\tau = F/bL$ or

$$\tau = \frac{2\alpha Gb}{L} r \sin\theta \quad (3.2)$$

When $\theta = \pi/2$, that is, when the dislocation segment forms a semicircle, the shear stress is maximum and equal to

$$\tau_{max} = \frac{2\alpha Gb}{L} \quad (3.3)$$

If the maximum necessary shear stress is acting on a dislocation segment pinned at two points, as in Figure 3.8, the semicircular form is soon attained, and the dislocation becomes unstable and expands indefinitely. The expanding loop doubles back on itself, as in (c) and (d), until two sections meet and annihilate each other, since they have the same Burgers

vector but opposite line sense, forming a closed outer loop that continues to expand and a new dislocation segment that will repeat the process [20,25].

Suppose that the length of the slip plane is s , and that an edge dislocation moves a distance x in the slip plane. Then it produces a displacement bx/s , so that n dislocations moving an average distance \bar{x} produce a displacement $u = nb\bar{x}/s$. If the average spacing between slip planes is l , then the plastic shear strain is:

$$\gamma^p = \frac{u}{l} = \frac{nb\bar{x}}{ls} \quad (3.4)$$

Where n/l is the total length of dislocation lines of the given family per unit of the crystal volume. This quantity is known as the density of dislocations and is denoted ρ . Since only the mobile dislocations contribute to plastic strain, their density ρ_m must appear in the equation for the plastic strain [20].

$$\gamma^p = \rho_m b \bar{x} \quad (3.5)$$

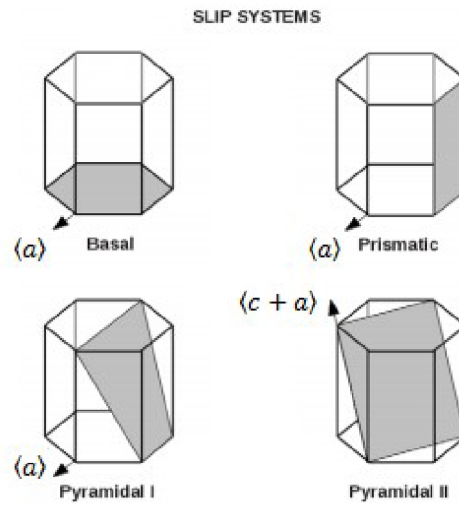
The plastic shear-strain rate is:

$$\dot{\gamma}^p = \rho_m b \bar{v} \quad (3.6)$$

Where \bar{v} is the average dislocation velocity [20].

Obstacles to dislocation motion include also interstitial and substitutional atoms, foreign particles, grain boundaries, external grain surface, and change in structure due to phase change. The dislocations can move past these obstacles, but only at higher stresses which leads to strengthening of the material [20,25].

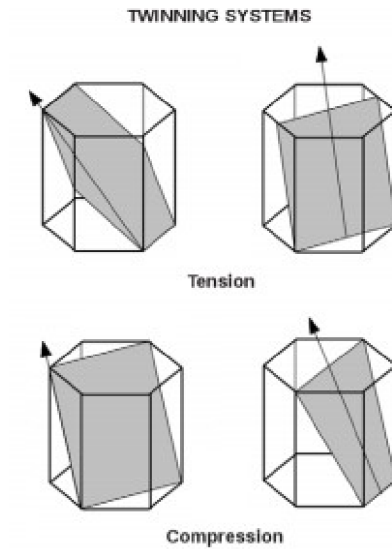
The magnesium's HCP structure accommodates the motion of dislocations along the (0001) basal, $\{\bar{1}100\}$ prismatic, and $\{\bar{1}101\}$ pyramidal planes in the $\langle 11\bar{2}0 \rangle$ directions, as shown in Figure 3.9. To accommodate compatible plastic strains in a polycrystalline metal five independent slip systems are required. Because these three slip systems have the same $\langle a \rangle$ direction, there are only four independent slip systems in magnesium. For compatible plastic strains, other than $\langle a \rangle$ type slip system must be activated. Typically this is accommodated by the $\langle c + a \rangle$ type slip system, as shown in Figure 3.9. However, generally, the shear stress required to activate this slip system is higher than that of the $\langle a \rangle$ type slip systems, leading to anisotropic plastic deformation behaviour at the single-crystal level. The shear stress required to activate the different slip systems in magnesium varies depending on the temperature and composition of the material. It seems that incompatible plastic strains in polycrystalline HCP metals can also be accommodated by the activation of deformation twinning [14].



Slip plane		Slip direction		Independent modes
Basal	(0001)	$\langle a \rangle$	$\langle 11\bar{2}0 \rangle$	2
Prismatic	$\{\bar{1}100\}$	$\langle a \rangle$	$\langle 11\bar{2}0 \rangle$	2
Pyramidal I	$\{\bar{1}101\}$	$\langle a \rangle$	$\langle 11\bar{2}0 \rangle$	4
Pyramidal II	$\{\bar{1}\bar{1}21\}$	$\langle c + a \rangle$	$\langle 11\bar{2}\bar{3} \rangle$	5

Figure 3.9 – Slip systems in magnesium [14,26].

3.2.2. Deformation by twinning



Type	Twinning plane	Twinning direction
Tension	$\{10\bar{1}2\}$	$\langle\bar{1}011\rangle$
	$\{11\bar{2}1\}$	$\langle\bar{1}\bar{1}26\rangle$
Compression	$\{11\bar{2}2\}$	$\langle11\bar{2}\bar{3}\rangle$
	$\{10\bar{1}1\}$	$\langle1\bar{1}12\rangle$

Figure 3.10 – Twinning systems in magnesium [14,26].

The second important mechanism of plastic deformation is twinning. Twinning generally occurs when slip is restricted. Thus, in HCP metals, twinning is the main deformation mechanism due to the limited number of slip systems. Twinning is based on the conjoint motion of atoms that shift in the same direction by the defined amount of shear strain along the same plane. The twinned portion of the crystal is a mirror image of the parent crystal. The plane of symmetry between the two portions is called the twinning plane and the direction of movement of the atoms is called the twinning direction. The most commonly activated twinning systems in magnesium are $\{10\bar{1}2\}\langle\bar{1}011\rangle$ and $\{11\bar{2}1\}\langle\bar{1}\bar{1}26\rangle$ for tensile loading along the c axis and $\{11\bar{2}2\}\langle11\bar{2}\bar{3}\rangle$ and $\{10\bar{1}1\}\langle1\bar{1}12\rangle$ for compressive loading as shown in Figure 3.10 [14].

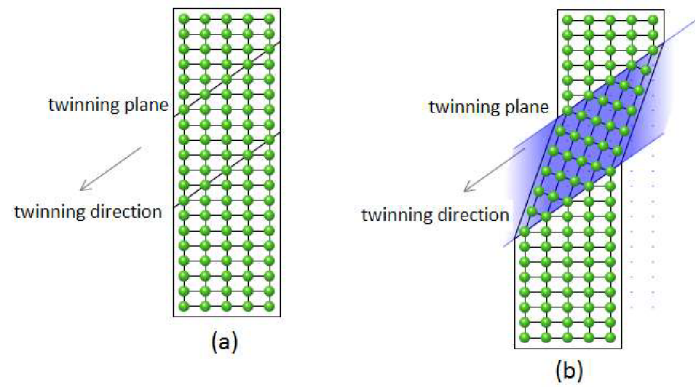


Figure 3.11 – Deformation by twinning, (a) undeformed crystal, (b) after deformation twinning [21].

Compared to slip, the process of twinning is extremely rapid (twin dislocations propagate with a speed approaching a speed of sound in the material) and can be divided into three stages: nucleation, propagation and thickening. Nucleation is a localized phenomenon which occurs on grain boundaries and is based on the interaction between grain boundaries and dislocations. Next stage is twin propagation. During propagation the twin grows in a thin, sharply pointed plate with a rapid increase in its diameter. It terminates once a twin impinges upon the boundaries of its parent grain or another obstacle. Twin propagation is accompanied by the relaxation of stresses inside the grain, and it is supposed that stress relaxation is one of the driving forces for twinning. The last stage is the twin thickening where the twin grows in thickness producing a lenticular shape until a stable twin aspect ratio is attained. The aspect ratio depends on applied stress. Twin thickening involves the motion of dislocations along the twin boundary [21,27]. The schematic illustration of twin growth associated with twinning dislocation is shown in Figure 3.12.

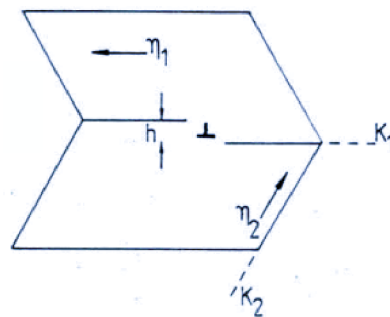


Figure 3.12 – Schematic illustration of a twinned crystal and the step associated with a twinning dislocation, K_1 is a twinning plane, η_1 is a twinning direction, K_2 is a conjugative twinning plane, and η_2 is a conjugative twinning direction [4].

Unlike slip, which is usually considered to occur in discrete multiples of the atomic spacing, in twinning the atom movements are much less than an atomic distance and every atomic plane is involved in the deformation (slip occurs on widely spread planes). The movement of the atoms in twinning is generating a twinning shear, which relaxes the stress in the lattice. The generated twinning shear in HCP metals depends on material and its c/a ratio [4]. The dependence is shown in Figure 3.13.

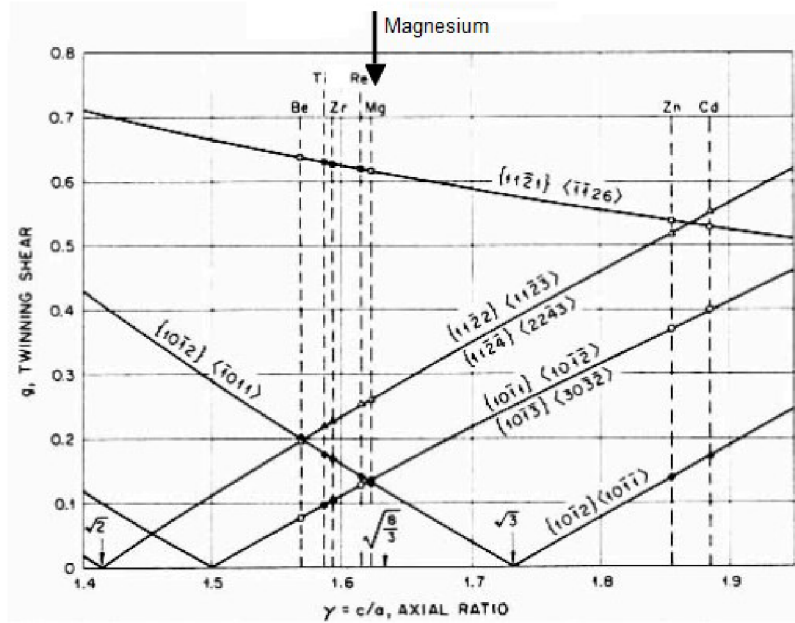


Figure 3.13 – Variation of twinning shear with the axial ratio in HCP metals, a filled symbol indicates an active twinning mode (for $\{10\bar{1}2\}\{1011\}$ extension twin in magnesium $g \approx 0,13$) [4].

Many variables such as temperature, strain rate, an amount of pre-strain, grain size, crystal orientation, alloy composition or precipitates are believed to influence the twinning behaviour. However, these variables seem to be highly material dependent (some of these variables seem to affect the twinning in particular materials, while in other materials the same variables show no influence on the twinning). The nature of the interaction between the twins and the precipitates was found to be dependent on the relative thickness of the twin and the precipitate. Twins were observed to engulf, bypass or impinge upon the precipitates, but the precipitates themselves were not twinned. In this thesis the twin and precipitate interaction will be investigated, considering the twin that impinges upon the precipitates [4,28].

4. Finite element method

The finite element method is a computational technique, used to obtain approximate solutions of the boundary value problems in engineering. Generally, a boundary value problem is a mathematical problem, which is usually described by partial differential equations together with a set of constraints, called the boundary conditions. In a majority of the problems associated with engineering, the partial differential equations cannot be solved by standard analytical methods due to the complexity of the problems. The finite element method subdivides the problem into smaller, simpler parts called the finite elements which allow transforming the original differential equations in a system of algebraic equations which can be solved by numerical methods. FEM then uses variation methods to approximate a solution by minimizing an associated functional. The FEM allows the solution of the problems associated with continuum mechanics (stress-strain analysis, modal analysis, and transient analysis), thermodynamics, fluid dynamics, electromagnetism etc [29,30].

4.1. The stress – strain analysis by FEM

The definition of the FE model includes the following steps:

- Geometric domain definition and its partition into FE mesh
- Selection of the proper type of elements
- Boundary conditions and loads definition
- Strain and constitutive behaviour definition

4.1.1. Mesh and elements

The geometric domain of the problem is subdivided creating the finite element mesh. The crucial parameter is the element size which has to be small enough to provide an accurate approximation of the problem solution. The sufficient element size is determined by the mesh convergence studies. The elements can be divided according to the shape and number of dimension of the domain: 1D problems can be solved by strut or beam elements, 2D geometries can be discretized by plane or shell elements and full 3D analysis can be performed by solid elements. The basic shape is a quadrilateral or a triangle (2D) and a brick or a tetrahedron (3D). The elements are also defined by the interpolation functions used for displacement calculations. There are linear and higher order elements (quadratic) (see Figure 4.1) [30].

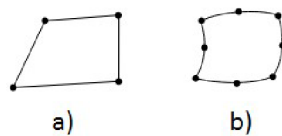


Figure 4.1 – The basic 2D elements – a) linear without mid-nodes, b) quadratic with mid-nodes.

4.1.2. Loads and boundary conditions

The boundary conditions and loads are sets of constraints that are applied to problem geometry. These constraints can be of two types: geometric, and force. Geometric constraints impose displacements to the surface of the body, and force constraints impose loading forces to the elements of the body. The load can be superficial or volumetric [30]. A general scheme of boundary conditions is shown in Figure 4.2.

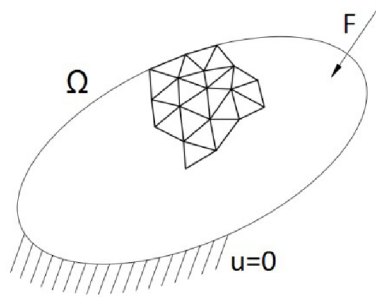


Figure 4.2 – Partially meshed geometric domain Ω with applied volumetric force and zero displacement.

Using the theory of continuum mechanics, it is possible to model the mechanical behaviour and the deformation of each element by simple mathematical equations. These equations involve the geometric relations, the equilibrium law, and the constitutional equations.

4.1.3. Strain definition

The deformation of the element can be described by the strain tensor (engineering strain).

$$\varepsilon_{ij} = \begin{pmatrix} \varepsilon_{11} & \gamma_{12} & \gamma_{13} \\ \gamma_{12} & \varepsilon_{22} & \gamma_{23} \\ \gamma_{13} & \gamma_{23} & \varepsilon_{33} \end{pmatrix} \quad (4.1)$$

Its components can be evaluated from displacements by the following equation.

$$\varepsilon_{ij} = \frac{1}{2} \left(\frac{\partial u_i}{\partial X_j} + \frac{\partial u_j}{\partial X_i} \right) \quad (4.2)$$

Where X_i refers to the undeformed shape and coordinates x, y, z and u_i refers to displacements in these axes for $i = 1, 2, 3$ [30].

4.1.4. The equilibrium law

If the body is in static equilibrium, the relation between the stress in the body and applied volumetric forces is given by the equilibrium law.

$$\frac{\partial \sigma_{ij}}{\partial x_j} + G_i = 0 \quad (4.3)$$

Where G_i is a component of the volumetric forces and σ_{ij} is the Cauchy stress tensor, which characterises the stress state in the element.

$$\sigma_{ij} = \begin{pmatrix} \sigma_{11} & \tau_{12} & \tau_{13} \\ \tau_{12} & \sigma_{22} & \tau_{23} \\ \tau_{13} & \tau_{23} & \sigma_{33} \end{pmatrix} \quad (4.4)$$

These stress and strain tensors are only valid for small strains (up to 10^{-2}) and are associated with the linear theory of elasticity. If the strains are large, it is necessary to use other tensors for the characterisation of the stress and deformation, for example, deformation gradient tensor, which is described in the next chapter and is used for characterisation of the large deformations [30].

4.1.5. The constitutive equations

The relation between the stress and strain in a particular material is governed by constitutive equations (sometimes referred to as material model). For a description of the behaviour of linear elastic material the generalised form of Hooke's law is used.

$$\sigma_{ij} = C_{ijkl}\varepsilon_{kl} \quad (4.5)$$

Where C_{ijkl} is stiffness tensor, which represents the material properties. In this tensor form, each stress component depends linearly on all strain components. Tensors representing material properties have 81 components, but due to symmetry and thermodynamical laws only 21 of the components are independent and needed for the full description of the anisotropic elastic properties. The tensor form of Hooke's law can be rewritten in matrix form using Voigt notation.

$$\begin{pmatrix} \sigma_{11} \\ \sigma_{22} \\ \sigma_{33} \\ \sigma_{23} \\ \sigma_{13} \\ \sigma_{12} \end{pmatrix} = \begin{pmatrix} C_{11} & C_{12} & C_{13} & C_{14} & C_{15} & C_{16} \\ C_{21} & C_{22} & C_{23} & C_{24} & C_{25} & C_{26} \\ C_{31} & C_{32} & C_{33} & C_{34} & C_{35} & C_{36} \\ C_{41} & C_{42} & C_{43} & C_{44} & C_{45} & C_{46} \\ C_{51} & C_{52} & C_{53} & C_{54} & C_{55} & C_{56} \\ C_{61} & C_{62} & C_{63} & C_{64} & C_{65} & C_{66} \end{pmatrix} \begin{pmatrix} \varepsilon_{11} \\ \varepsilon_{22} \\ \varepsilon_{33} \\ 2\varepsilon_{23} \\ 2\varepsilon_{13} \\ 2\varepsilon_{12} \end{pmatrix} \quad (4.6)$$

Other material models, which describe other types of material behaviour, may also be used. For example: viscoelastic, hyperelastic, plastic or vicoplastic behaviour, and crystal plasticity models [30].

4.1.6. FEM solution methods for elastic material

The solution is obtained by the calculation of displacements in every node. The deformed shape of the loaded and constrained body is clearly defined by the **minimum total potential energy principle**. It formulates a general natural principle that from all the possible deformed shapes, only the one with the lowest energy will occur. The elastic potential energy of the loaded and constrained body Π is the sum of the elastic strain energy W stored in the deformed body and the potential energy P associated with the applied forces [30].

$$\Pi = W - P \quad (4.7)$$

$$W = \frac{1}{2} \int_{\Omega} \sigma^T \cdot \varepsilon \cdot dV \quad (4.8)$$

$$P = \int_{\Omega} u^T \cdot o \cdot dV + \int_{\Gamma_p} u^T \cdot p \cdot dS \quad (4.9)$$

Where σ is the stress, ε is the strain, and o and p are applied volumetric and surface forces. It also generally depends on the continuous functions of displacements $u(x, y, z)$. The approximate functions of displacements in FEM are expressed as the sum of the basis functions N_i multiplied by the values of displacements in the nodes u_i . The basis function is an element of a particular basis for a function space. Every continuous function space can be represented as a linear combination of the basis functions [30].

$$u(x, y, z) \approx \sum_{i=1}^l N_i(x, y, z) \cdot u_i \quad (4.10)$$

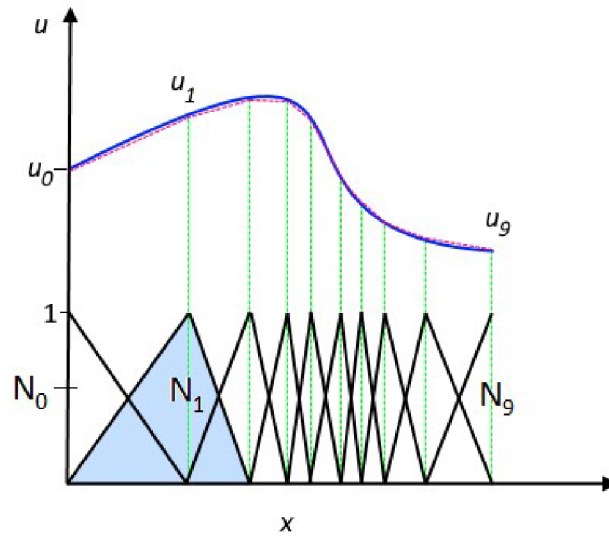


Figure 4.3 – Approximation of the displacement function u [29]

Mathematical variation methods make it possible to find the approximate function of the displacements by finding the minimum of the elastic potential energy Π , thus to find the displacements in every node, corresponding to the real deformed shape of the body. The minimum is found by setting the partial derivative of the elastic potential energy with respect to the displacements to zero.

$$\frac{\partial \Pi}{\partial u_i} = 0 \quad (4.11)$$

The elastic potential energy is a sum of the strain energy and potential energy associated with the loads. By the derivation, these energies are transformed into forces, so the produced function is the equilibrium of internal and loading forces. At each node, the strains are evaluated from the geometric relations and the stresses are evaluated from constitutive equations. The system of algebraic equations obtained by minimizing the elastic potential energy can be solved by direct numerical methods such as Gauss elimination or Cholesky decomposition. Solving of non-linear problems is carried out by iterative methods such as Newton-Raphson method [30].

5. Objectives

The mechanisms of twin and precipitate interaction are very complex. The twin was observed to bypass, engulf, or impinge upon precipitates during propagation [28]. The interaction between twin and engulfed precipitates during twinning was discussed by Robson [31]. In this thesis, the interaction between twin and precipitates during the twin thickening process is investigated for the case in which the twin impinges upon the precipitate. The $\{10\bar{1}2\}\langle\bar{1}011\rangle$ extension twinning in magnesium is considered for the analysis. Due to the transformation of the lattice during twinning, a back stress is generated and relaxes the stress associated with the initial loads. The twin thickens until the certain stable aspect ratio. It is believed that the stable aspect ratio is attained when the generated back stress zeroes the initial stress. In reverse, it is possible to evaluate approximate initial shear stress values, required to stabilize a twin of a given aspect ratio [27]. The task is to analyse the stress fields induced by the twinning depending on the size of the precipitates. Another task is to analyse the initial shear stresses values for accommodating twins with different aspect ratios embedded by precipitates with different thicknesses. The stress level inside the twin is evaluated by its average value and by the value at the centre of the twin boundary. The former variable describes overall stress state while the latter describes the driving force for the twinning dislocations that nucleate at the twin boundary and alter the twin shape [27]. The main goals of this analysis are:

- Creation of 2D FEM model of twin and precipitates in lattice
- Analysis of induced fields depending on size and layout of the precipitates and different values of critical shear stresses
- Proposition and discussion of the mechanisms of interaction and their influence on twin growth

6. Numerical model definition

6.1. Topology and geometry of the twin and precipitates

As it was mentioned in Chapter 3, deformation twinning produces lenticular shape twins. The $\{1012\}\langle 10\bar{1}1\rangle$ extension twin will be considered for the analysis. The precipitates in magnesium alloys form most often rod and plate like shapes. The rod shaped precipitates will be considered for the analysis [27,32]. For each twin, three precipitate thicknesses relative to the twin thickness will be considered.

6.2. Model of the geometry

The geometry is modelled as two dimensional. The global coordinate system is associated with the HCP magnesium cell unit system in a way that crystal c -axis coincides with global X -axis.

The twin is modelled as an elliptical inclusion with two square shaped precipitates at each tip of the twin in a large domain, representing a basic material. The model of geometry is shown in Figure 6.1. The elliptical shape is a close approximation of the real lenticular one. Its advantage is that such geometry can be validated by analytical solution. Square shaped precipitates are also a close 2D approximation of rods or plates. The $\{1012\}\langle 10\bar{1}1\rangle$ extension twin is inclined by angle 46.84° with respect to the X -axis which results from the crystal lattice constants ($a = 0.321$ nm, $c = 0.521$ nm). The size of the domain is set to be large enough in order to minimize the influence of boundary conditions. Nine models of geometries are considered for the analysis, obtained by variation of twin thickness and precipitate thickness. Specific values of the used geometric parameters are shown in Table 6.1.

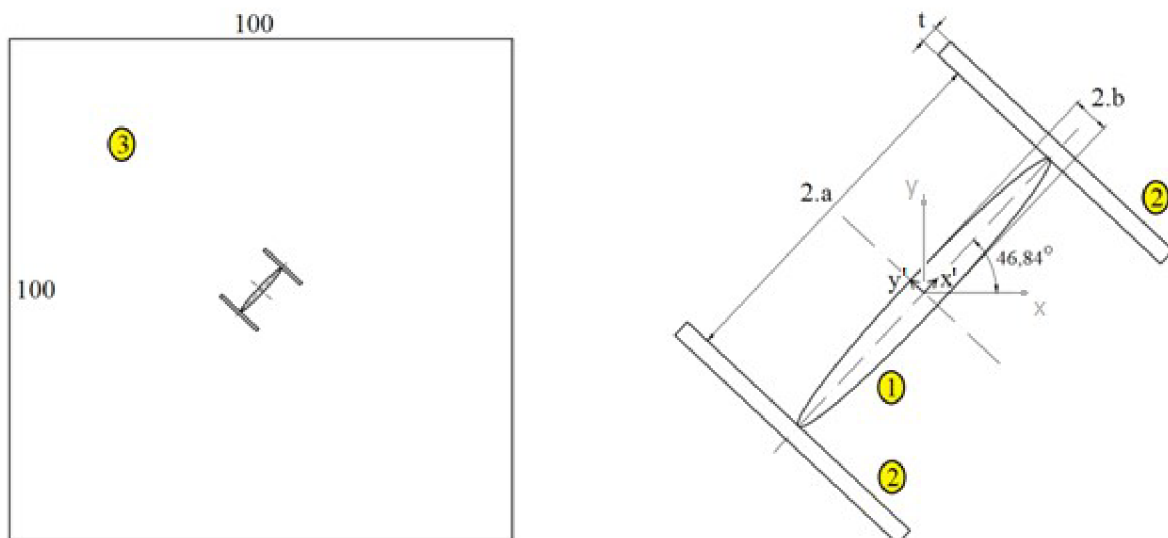


Figure 6.1 – Model of geometry of twin (1) and precipitates (2) in lattice (3). The x axis is parallel to the HCP c axis.

Twin length a [unit]	6
Twin thickness b [unit]	$a/20, a/10, a/5$
Precipitate thickness t_p [unit]	$b/2, b, 2b$

Table 6.1 – Specific values of the geometric parameters.

6.3. Boundary conditions and loading

Boundary conditions are illustrated in Figure 6.2. The domain is considered as a uniformly stressed region inside magnesium alloy. The edges of the domain are forced to be straight during deformation which models the influence of the surrounding of the domain. The edges are also anchored in their middles in order to prevent the rigid body motion.

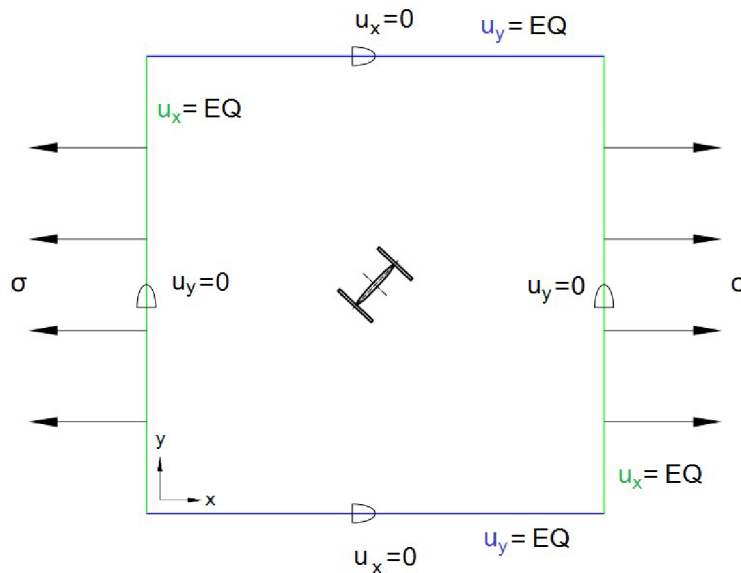


Figure 6.2 – Scheme of the boundary conditions and loads.

Loading of the system is applied in two steps. The domain is at first loaded by the external tensile stress of the certain level as shown in Figure 6.2. The external stress level is then kept constant during the simulation. The upper limit for the tensile stress is given by the activation of the plasticity in the domain. The domain is supposed to be in pure elastic state prior twinning. Particular values are shown in Table 6.2. The twinning shear is activated in the second step by an application of pseudo thermal shear strain using orthotropic thermal expansion coefficient [27]. The value of the coefficient is set to produce shear with a value of 0.13. The schematic representation of twin shear is shown in Figure 6.3.

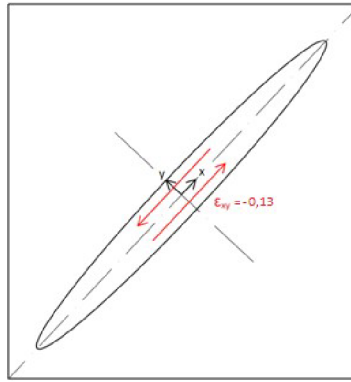


Figure 6.3 – Shear strain load.

Twin aspect ratio b/a	Applied stress values [MPa]				
	0.05	200	250	300	370
0.1		300	350	400	440
0.2		380	410	425	440

Table 6.2 – The values of the applied stress.

6.4. The material model

The elastic properties of magnesium polycrystalline aggregate are fairly isotropic. However, at a single crystal level, the magnesium shows elastic anisotropy due to its HCP crystal structure [20]. The twin is modelled as anisotropic elastic material. The anisotropic linear elastic behaviour is characterised by the stiffness tensor with 9 non-zero components. The rotation of elastic material properties during twin transformation is modelled by the temperature dependence of the elastic constants. The material of the precipitates is considered to be isotropic and elastic. The plasticity of the lattice is modelled within the crystal plasticity framework.

6.4.1. The material model based on the crystal plasticity theory

The crystal plasticity model is based on a decomposition of the deformation gradient tensor F into elastic and plastic parts and is defined as transformation between original and deformed geometry [30].

$$F = F^e F^p \tag{6.2}$$

The deformation gradient tensor can be written in matrix form:

$$F = \begin{bmatrix} \frac{\partial x_1}{\partial X_1} & \frac{\partial x_1}{\partial X_2} & \frac{\partial x_1}{\partial X_3} \\ \frac{\partial x_2}{\partial X_1} & \frac{\partial x_2}{\partial X_2} & \frac{\partial x_2}{\partial X_3} \\ \frac{\partial x_3}{\partial X_1} & \frac{\partial x_3}{\partial X_2} & \frac{\partial x_3}{\partial X_3} \end{bmatrix} \quad (6.3)$$

Its components are stretches

$$\lambda_{ij} = \frac{\partial x_i}{\partial X_j} \quad (6.4)$$

Where x_i refers to the coordinates of the deformed geometry and X_j refers to the coordinates of the original geometry for $i, j = 1, 2, 3$. The plastic part of the deformation gradient is related to the slip occurring in slip systems characterised by slip direction m^s and normal to the slip plane n^s .

$$\dot{F}^P F^{P-1} = \sum_{s=1}^n \dot{\gamma}^s m^s \otimes n^s \quad (6.5)$$

Slip rate on the given slip system $\dot{\gamma}^s$ is defined by the following expression:

$$\dot{\gamma}^s = \left\langle \frac{|\tau^s - x^s| - r^s}{K} \right\rangle^n \text{sign}(\tau^s - x^s) \quad (6.6)$$

Where τ^s is the resolved shear stress, which acts on the given slip plane, K and n are parameters of the Norton's law, parameters x^s , r^s are associated to the isotropic and kinematic hardening. A non-linear hardening rule is given by the following equation.

$$r_s = r_0 + q \sum_{r=1}^n h^{sr} (1 - \exp(-bv^r)) \quad (6.7)$$

Where r_0 is the initial value of critical resolved shear stress, q and b are phenomenological constants, v^r is the cumulated plastic slip for a system r . Slip systems interaction is described by the hardening matrix h^{sr} [27,34]. Presented crystal plasticity model is implemented in the FE code Z-set which was used for the simulations.

6.4.2. Input data

The magnesium elastic constants of the stiffness tensor are shown in Table 6.3. The material characteristics of magnesium for the crystal plasticity material model are shown in Table 6.4 and 6.5. The parameters represent an alloy AZ31 with the grain size of 5 μ m. Material

MASTER'S THESIS

parameters are taken from Siska et al. [27]. The precipitates are considered isotropic linear elastic with Young's modulus $E = 80$ GPa and the Poisson's ratio $\mu = 0.35$ [31].

Tensor component	C_{1111}	C_{2222}	C_{3333}	C_{1212}	C_{2323}	C_{3131}	C_{1122}	C_{2233}	C_{3311}
Value [GPa]	59.7	59.7	61.7	16.8	16.4	16.4	26.2	20.8	20.8

Table 6.3 – The used magnesium elastic constants.

K [MPa.s]	n	q [MPa]	b	h^{sr}
1.0	25.0	1.0	10.0	1.0

Table 6.4 – Coefficients used for the crystal plasticity FEM model.

Grain size	τ_0 basal [MPa]	τ_0 prismatic [MPa]	τ_0 pyramidal [MPa]
5 μm	46.4	95.2	177.7

Table 6.5 – Initial critical resolved shear stress values.

7. Results

7.1. Mesh convergence

To provide an accurate approximation of the problem solution the element size has to be sufficiently small. As it was shown in Chapter 6, the model of geometry consists of four parts: twin, which is modelled as an ellipse, two rectangular precipitates on each tip of the twin, and a large square shaped domain, in which twin and precipitates are situated. The location of the twin and precipitate interface is critical in terms of stress concentration. The mesh convergence is realised considering the shear stress values around the critical location using the ANSYS Mechanical APDL FEM software.

7.1.1. Model setting

The mesh convergence is carried out for three geometries, with the values of the geometric parameters, which are shown in Table 7.1.

Geometry number	1	2	3
Twin length a [unit]	6	6	6
Twin thickness b [unit]	$a/20$	$a/10$	$a/5$
Precipitate thickness t_p [unit]	$b/2$	$b/2$	$b/2$

Table 7.1 – Values of the geometric parameters of the geometries used for mesh convergence.

Each model of geometry is divided into several areas, because of better meshing capabilities (Figure 7.1). The entire geometry is then meshed using 2D quadratic plane elements. Material was considered isotropic linear elastic, with Young's modulus $E = 45$ GPa and Poisson's ratio $\mu = 0,35$. For mesh convergence, this material model was used for modelling both magnesium structures (twin and lattice) and precipitates, so the influence of precipitates wasn't included. The model was constrained with zero displacements at the domain edges and the only load was introduced by thermal shear strain in the twin. The analysis is static structural with the plane strain condition.

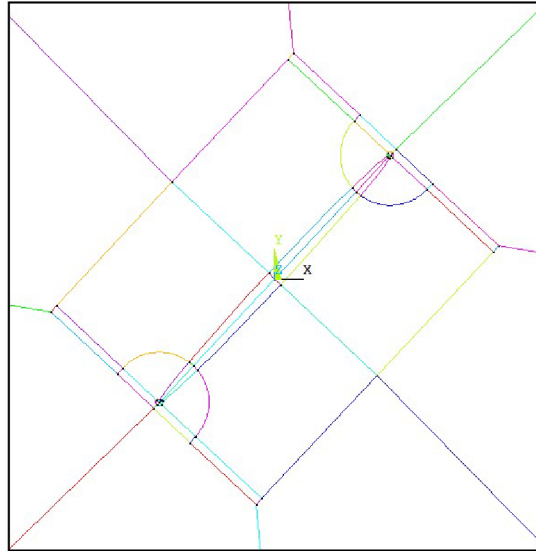


Figure 7.1 – The model of geometry in ANSYS (detail).

7.1.2. Element size influence on X'Y' shear stress and strain

Dependence of element size on shear stress was investigated in three points, which are shown in Figure 7.3. The points are situated around the location of twin and precipitate interface. Results are shown in Figures 7.4 - 7.6. Percentage differences between shear stresses depending on element size are shown in Table 7.2. The dependence of element size on shear strain was investigated only in point 1 and is shown in Figure 7.7.

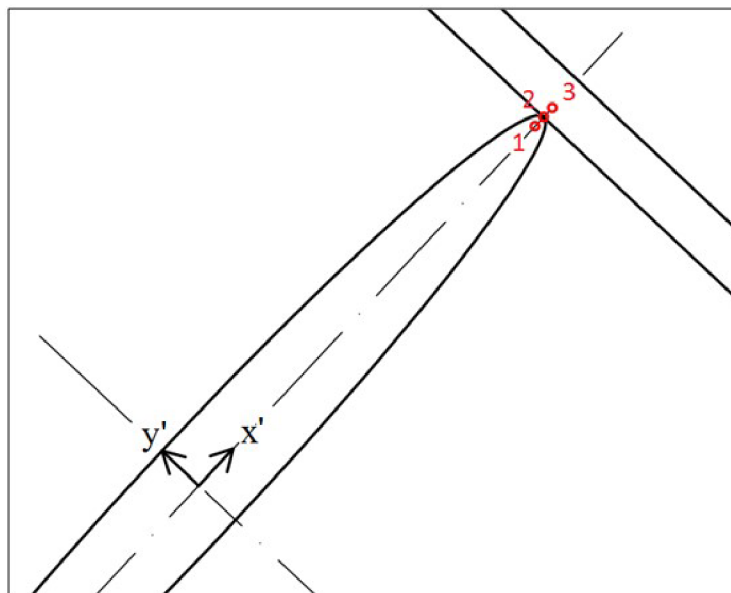


Figure 7.3 – Points for mesh convergence analysis.

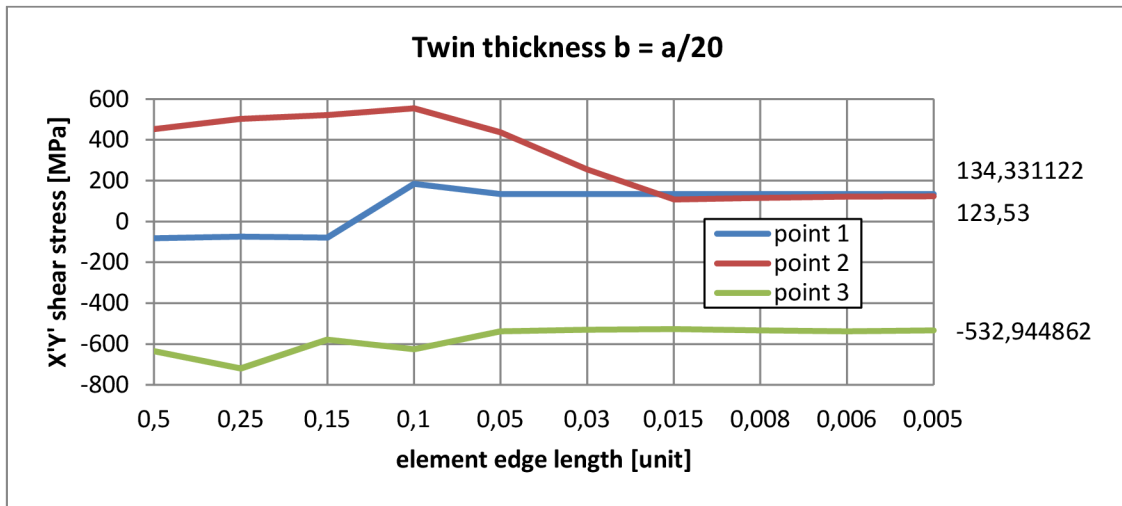


Figure 7.4 – The element size dependence on $X'Y'$ shear stress in geometry 1.

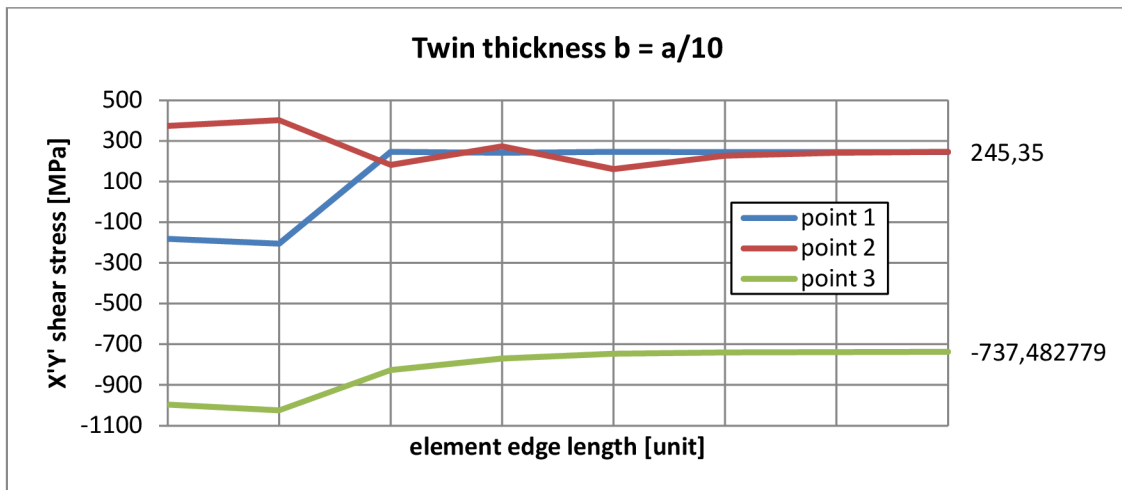


Figure 7.5 – The element size dependence on $X'Y'$ shear stress in geometry 2.

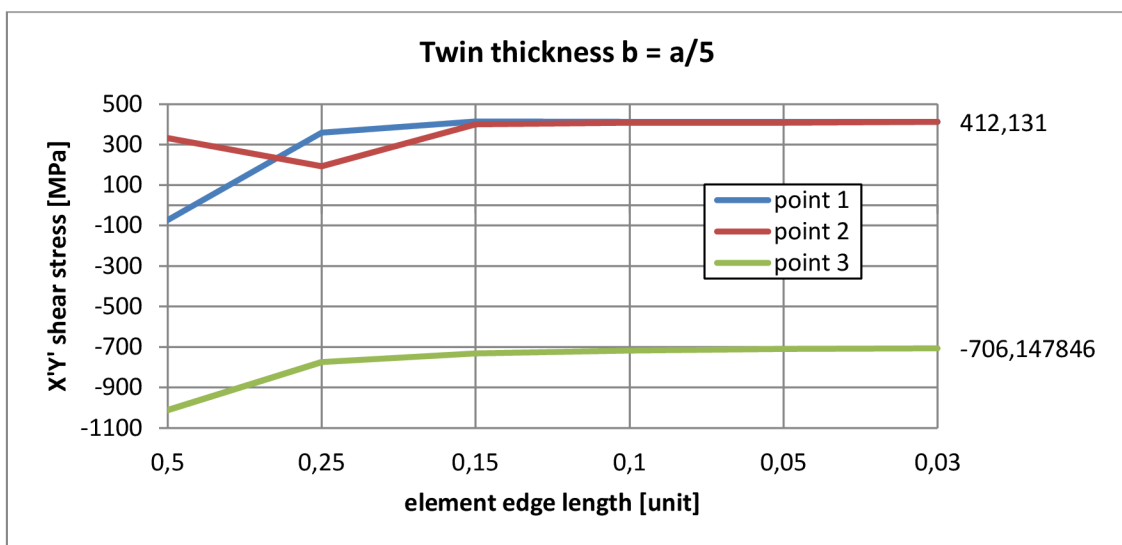


Figure 7.6 – The element size dependence on $X'Y'$ shear stress in geometry 3.

Element size [unit]	0,5 - 0,25	0,25 - 0,15	0,15 - 0,1	0,1 - 0,05	0,05 - 0,03	0,03 - 0,015	0,015 - 0,008	0,008 - 0,006	0,006 - 0,005
Geometry 1, point 2	11.3	3,7	6.3	21.3	41.6	57.8	7	6	1.3
Geometry 2, point 2	7.6	55	50.8	40.9	40.6	6.3	1.9		
Geometry 3, point 2	42.1	107.6	2.3	0.1	1.1				

Table 7.2 – Percentage differences between X'Y' shear stresses depending on element size [%].

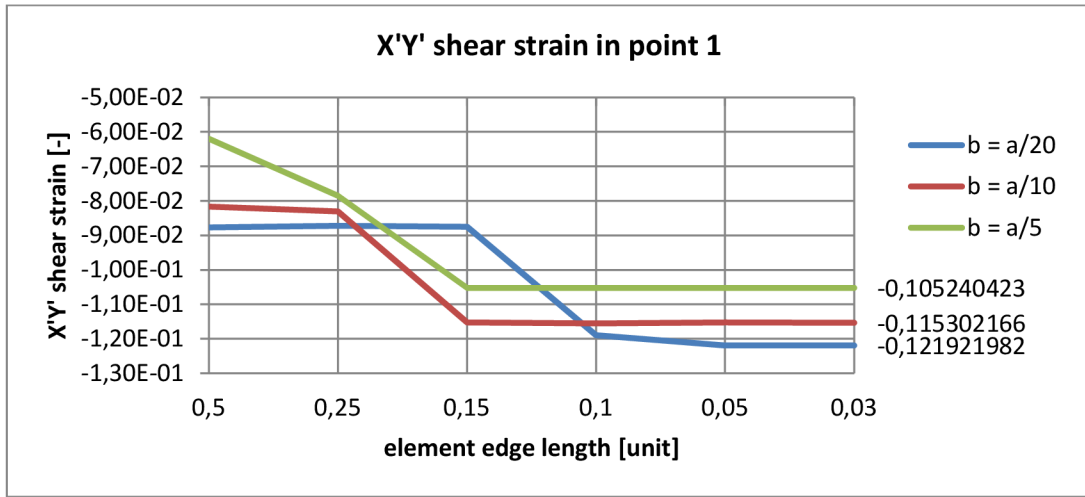


Figure 7.7 – Element size dependence on X'Y' shear strain in point 1.

7.1.3. Validation of the numerical model

An elliptical inclusion under internal shear strain in a homogenous isotropic matrix can be analytically analysed using Eshelby theory [33]. Resulting elastic strain in the inclusion is defined by the relation:

$$\varepsilon_{ij}^C = S_{ijkl} \varepsilon_{kl}^T \quad (7.1)$$

Where the resulting strain in the inclusion is ε_{ij}^C , S_{ijkl} is Eshelby's tensor, and ε_{kl}^T is an initial induced strain in the inclusion. Eshelby also found, that, stress and strain fields are homogeneous in the elliptical inclusion. Eshelby's tensor for the elliptical cylinder is used for validation of the numerical solution and its shear component is stated by the equation:

$$S_{1313} = \frac{a^2 + b^2 + (1 - 2\mu)(a + b)^2}{2(1 - \mu)(a + b)^2} \quad (7.2)$$

Where a represents the length of the ellipse, b represents the thickness of the ellipse, and μ is Poisson's ratio. The comparison of analytical and numerical solutions of resulting shear strains (numerical solution in point 1) are shown in Table 7.3 and Figure 7.8.

	FEM [-]	Analytical [-]	Error [%]
Geometry 1	-0.122	-0.1209	0.9
Geometry 2	-0.115	-0.1135	1.3
Geometry 3	-0.105	-0.1022	2.7

Table 7.3 – The comparison of resulting shear strains in the inclusion obtained by FEM and Eshelby's theory.

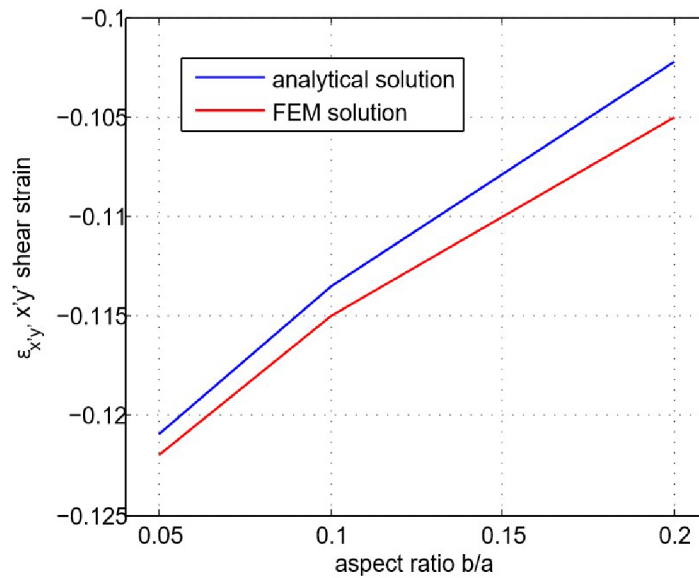


Figure 7.8 – The graph, showing the dependence of the resulting shear strain on the aspect ratio of the elliptical inclusion obtained by FEM and Eshelby's theory.

7.1.4. Mesh density setting

The mesh convergence study showed that the sufficient element size in the investigated location varies with different twin thickness. For meshing the global geometry, four sub domains were created (see Figure 7.4), and the element sizes in these sub domains were chosen considering the integrity of the mesh and the results from the mesh convergence study (large differences between element sizes would corrupt the mesh). The values shown in Table 7.4 are used to mesh all the nine models of geometries defined in Section 7.1.2. Additional mesh refinement would not lead to significant result changes, but the computation time would be unnecessarily increased. Details of the mesh of one of the models of geometry are shown in Figure 7.10.

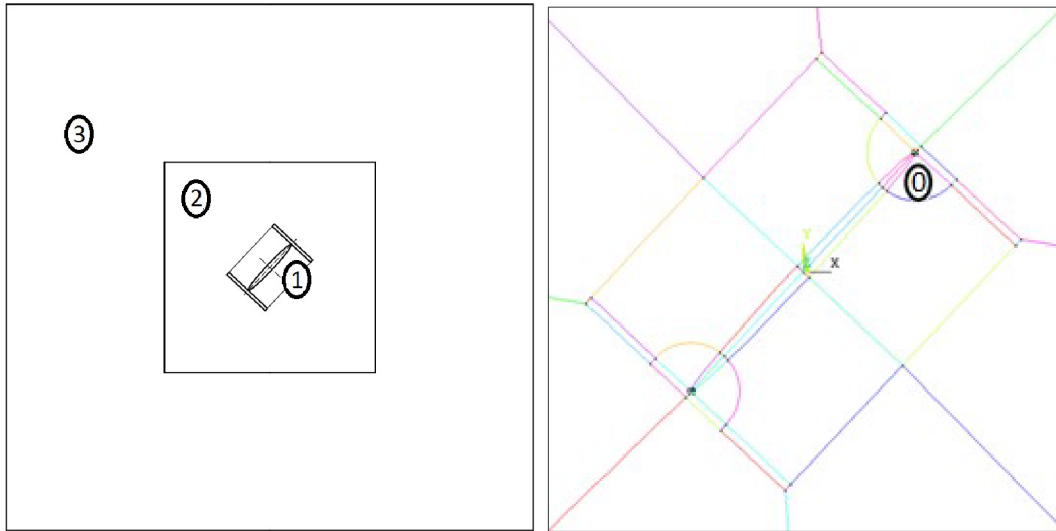


Figure 7.9 – The sub domains considered for meshing.

Location	Twin and precipitate contacts	Transient location (0)	Twin, precipitates, nearby region (1)	Further regions (2) and (3)	
	[units]	[units]	[units]	[units]	
Geometry 1	0.006	0.006 – 0.1	0.2	0.2 – 1	2
Geometry 2	0.015	0.015 – 0.1	0.2	0.2 – 1	2
Geometry 3	0.05	0.05 – 0.1	0.2	0.2 – 1	2

Table 7.4 – Particular element sizes in the sub domains.

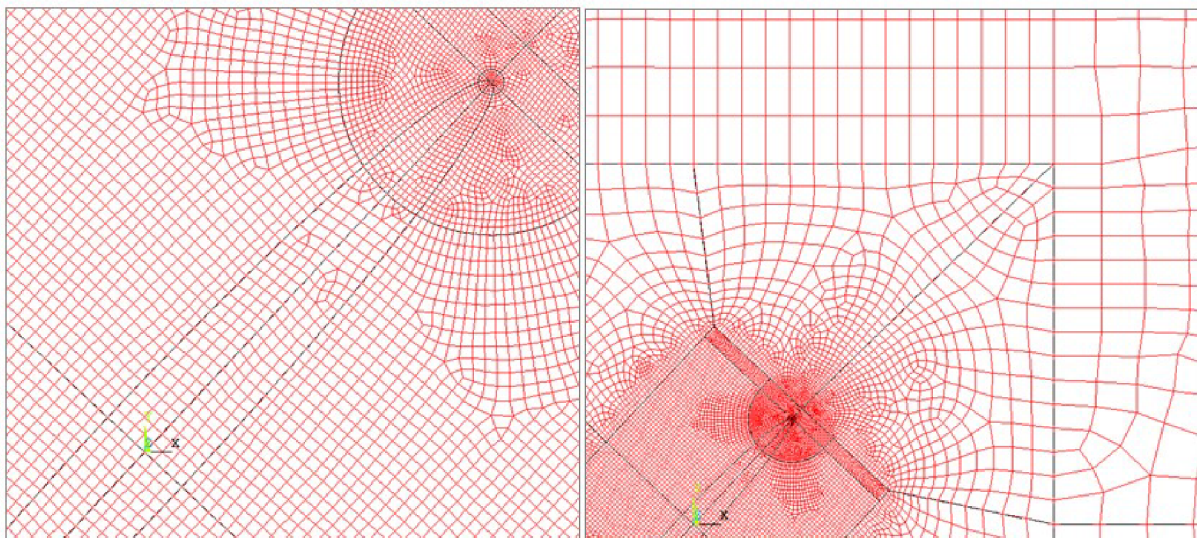


Figure 7.10 – Detailed view of the meshed geometry.

7.2. Numerical analysis of the twin and precipitate interaction

The analysis is realised in Z-set FEM software, and is based on the evaluation of the shear stress in the twinning plane. The stress in the twin is characterised by the boundary stress (Figure 7.11, red circle), and the twin average stress. The boundary stress is evaluated from a point which is situated on the twin boundary and is assigned as τ_B . The twin average stress is denoted τ_{TW} . The initial shear stress in the twin is evaluated from the loading stress using the Schmid's law:

$$\tau_r = \sigma \cos(\phi) \cos(\lambda) \quad (7.3)$$

Where τ_r is the initial resolved shear stress in the twin plane and twinning direction, σ is the load stress, ϕ is the tilt angle of the twinning plane, and λ is the tilt angle of the twinning direction. The initial resolved shear stress values for given equilibrium twin aspect ratios are read of the plots from the intersections between the stress curves and zero lines and are marked as τ_i .

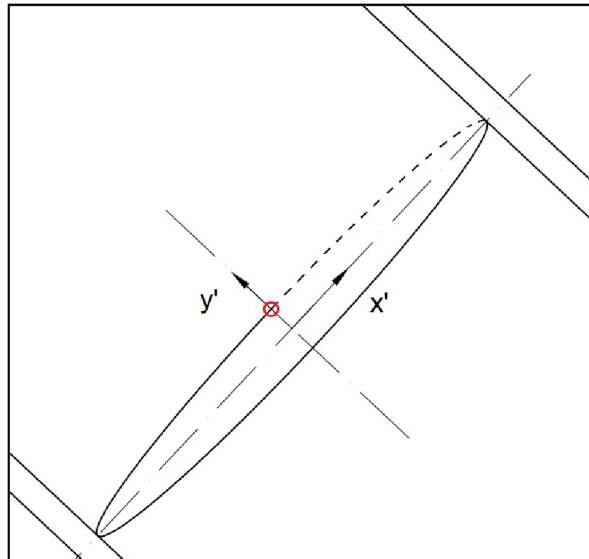


Figure 7.11 – Locations for the $x'y'$ shear stress evaluations.

7.2.1. Twin average results

The stress results for different aspect ratios and precipitate thicknesses are plotted against the resolved shear stresses in Figures 7.12 – 7.14. The evolution of the equilibrium twin aspect ratio with respect to the initial shear stress and relative precipitate thicknesses is shown in Figure 7.15. The values of the precipitate thicknesses are relative to the twin aspect ratio. However, it is possible to plot the curves with respect to the absolute values of the precipitate thicknesses. Such curves are shown in Figure 7.16.

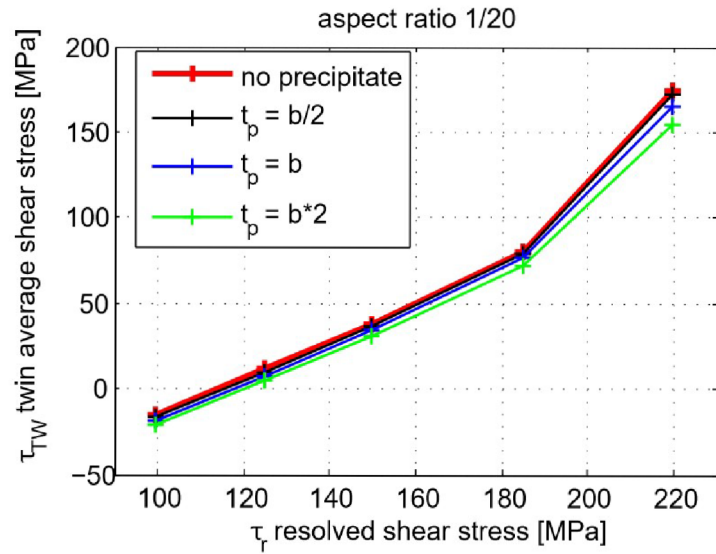


Figure 7.12 - τ_r - τ_{TW} shear stress curves of the average twin stress results for the twin aspect ratio 1/20 and precipitate thicknesses related to the aspect ratio.

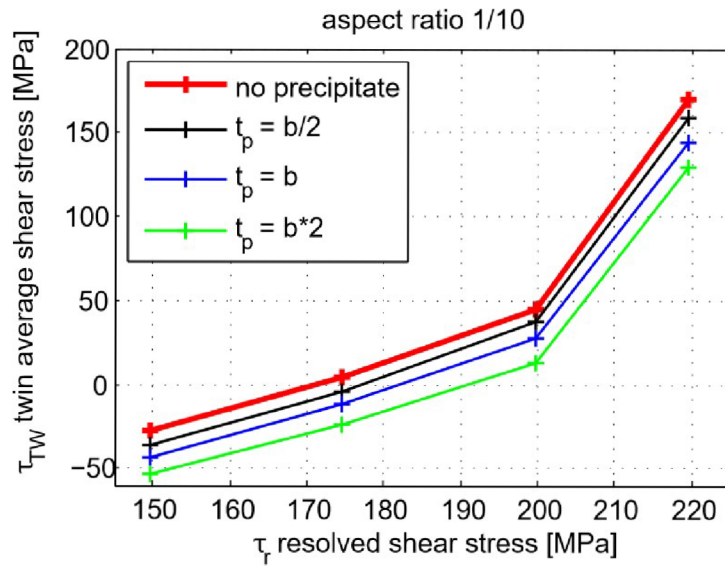


Figure 7.13 - τ_r - τ_{TW} shear stress curves of the average twin stress results for the twin aspect ratio 1/10 and precipitate thicknesses related to the aspect ratio.

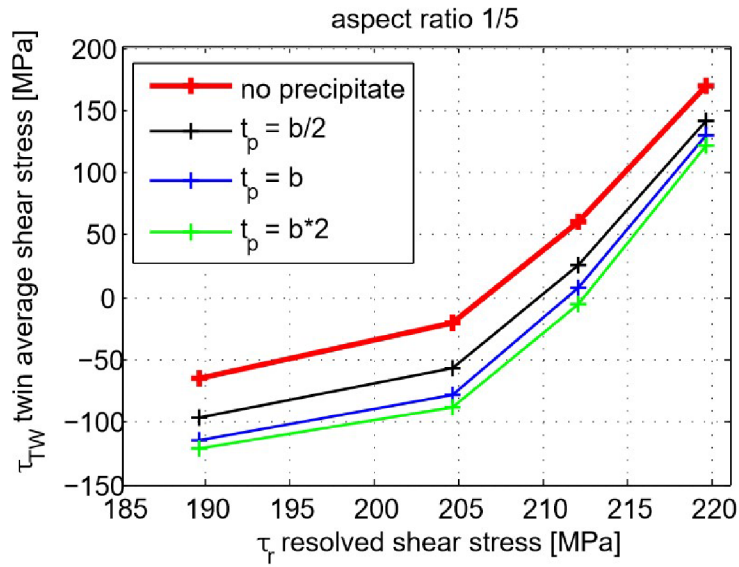


Figure 7.14 - τ_r - τ_{TW} shear stress curves of the average twin stress results for the twin aspect ratio 1/5 and precipitate thicknesses related to the aspect ratio.

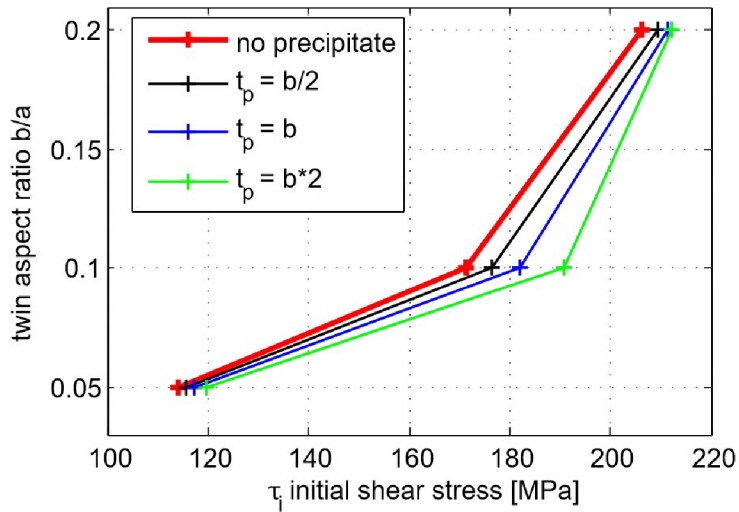


Figure 7.15 – The dependence of the equilibrium twin aspect ratio on the initial shear stress for average twin stress results with respect to the relative precipitate thicknesses.

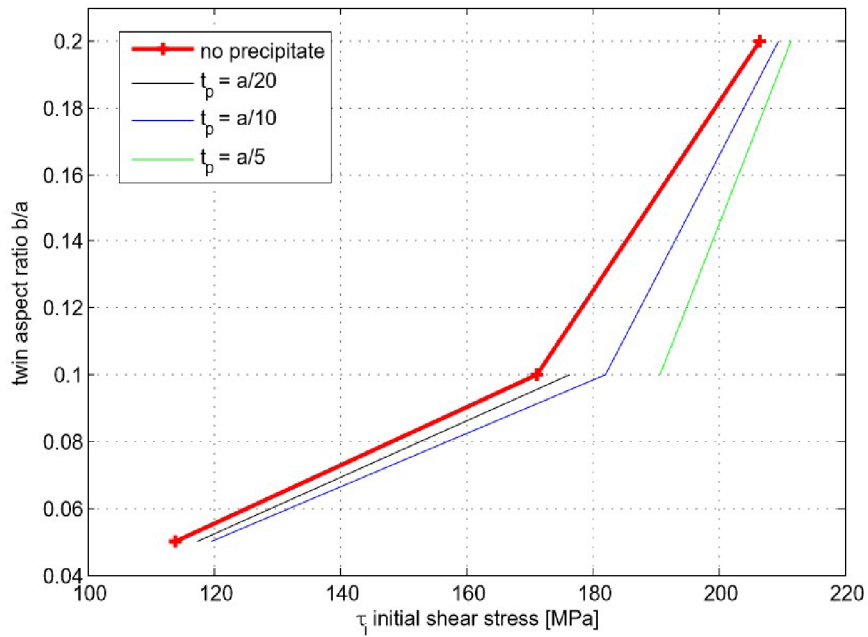


Figure 7.16 – The dependence of the equilibrium twin aspect ratio on the initial shear stress for average twin stress results with respect to the absolute precipitate thicknesses.

7.2.2. Twin boundary results

The boundary stress values for different aspect ratios and precipitate thicknesses are plotted against the resolved shear stresses in Figures 7.17 – 7.19. The projection of the $x'y'$ shear stress along the twin boundary (see Figure 11 – dashed line) to the x' axis is shown in Figure 7.20.

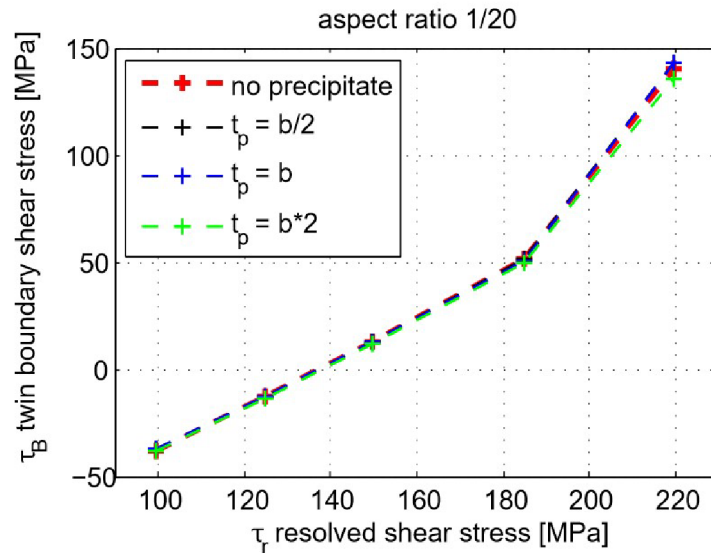


Figure 7.17 - τ_r - τ_B shear stress curves of the boundary twin stress results for the twin aspect ratio 1/20 and precipitate thicknesses related to the aspect ratio.

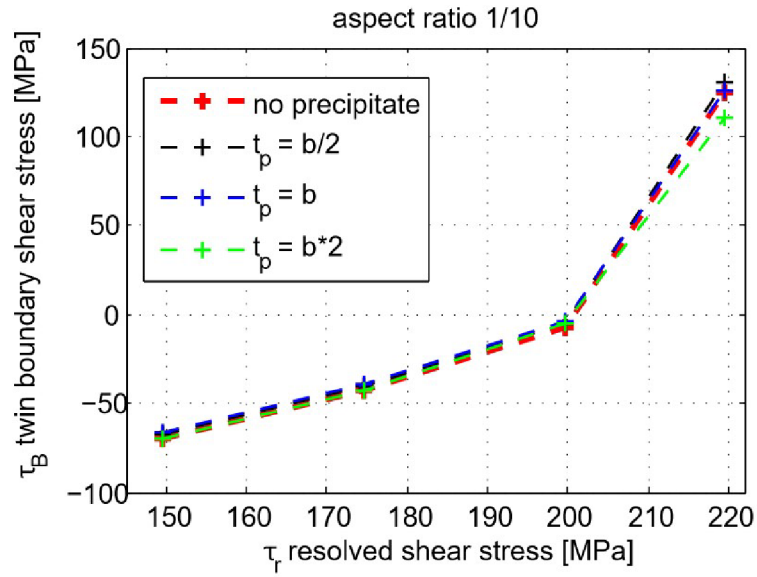


Figure 7.18 - τ_r - τ_B shear stress curves of the boundary twin stress results for the twin aspect ratio 1/10 and precipitate thicknesses related to the aspect ratio.

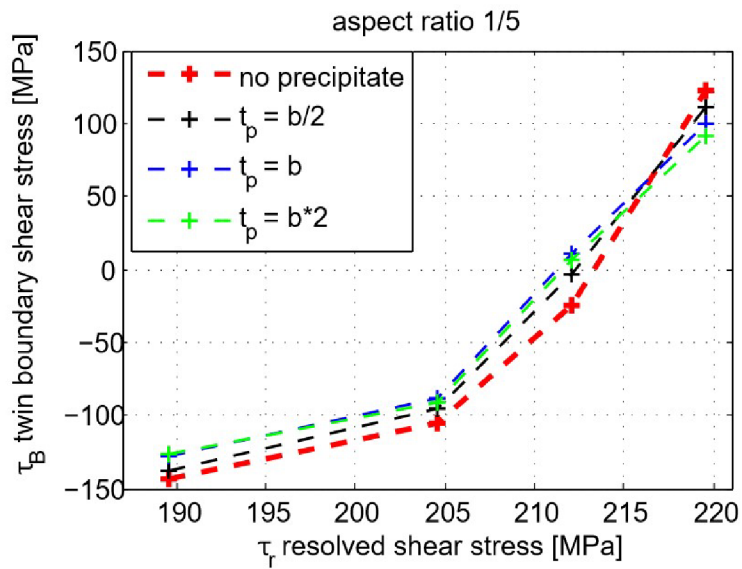


Figure 7.19 - τ_r - τ_B shear stress curves of the boundary twin stress results for the twin aspect ratio 1/5 and precipitate thicknesses related to the aspect ratio.

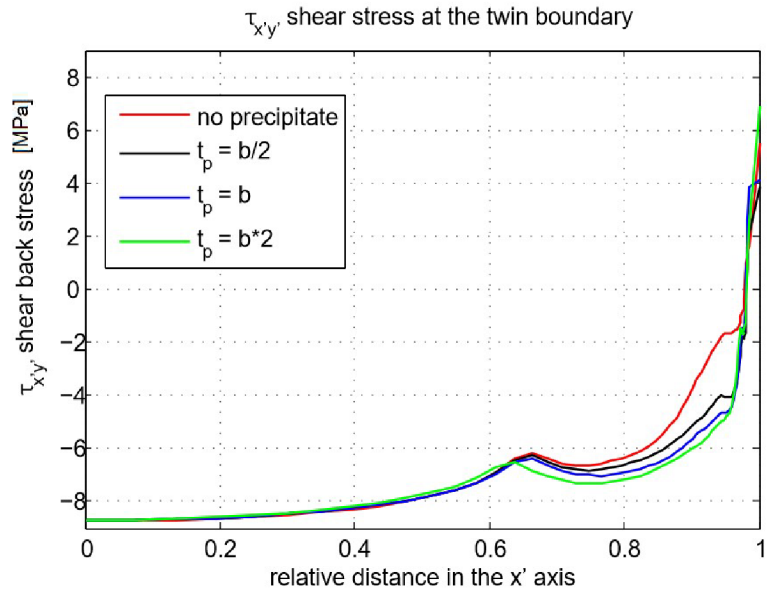


Figure 7.20 - $\tau_{x'y'}$ shear stress curves of the boundary twin results along the boundary projected to the x' axis for the twin aspect ratio 1/20 and precipitate thicknesses related to the aspect ratio ($\tau_r = 0$).

8. Discussion

The numerical study of the interaction between twins and precipitates in magnesium alloys during the twin thickening was proposed by Robson [31]. He suggested that twinning is suppressed by the precipitates. This observation is consistent with the results presented in this thesis.

The initial shear stresses for equilibrium twin aspect ratios estimated from average twin stress increases with relative precipitate thickness as shown in Table 8.1. On the other hand, initial stress values estimated from the twin boundary do not depend on the precipitates relative thickness (see Table 8.2). Such a discrepancy shows that the main effect of precipitates on the twin stress is focused in twin tip area. This is clearly illustrated in Figure 8.1 which shows the map of the twin shear stress for the same level of the initial stress. The shear stress in the twin tip area is decreasing with increasing thickness of the precipitate which results in a decreased average stress value.

	$t_p = 0$	$t_p = b/2$	$t_p = b$	$t_p = 2b$
$b/a = 0.05$	113.99 MPa	115.875 MPa	117.45 MPa	119.75 MPa
$b/a = 0.1$	171.3 MPa	176.3 MPa	182 MPa	190.83 MPa
$b/a = 0.2$	206.45 MPa	209.6 MPa	211.45 MPa	212.4 MPa

Table 8.1 –Initial shear stress results τ_i obtained from the average twin stress results, for given twin aspect ratios and precipitate thicknesses.

	$t_p = 0$	$t_p = b/2$	$t_p = b$	$t_p = 2b$
$b/a = 0.05$	137.5 MPa	137.1 MPa	137.25 MPa	138.1 MPa
$b/a = 0.1$	200.725 MPa	200.37 MPa	200.24 MPa	200.53 MPa
$b/a = 0.2$	213.3 MPa	212.25 MPa	211.25 MPa	211.6 MPa

Table 8.2 –Initial shear stress results τ_i obtained from the point at the twin boundary, for given aspect ratios and precipitate thicknesses.

Most significant effect of the precipitate thickness on the stress τ_i is observed for aspect ratio 0.1. This can be explained by the following reasoning. Presence of the precipitate restricts the possibility of stress relaxation by slip around the twin tip. Twins with aspect ratio 0.05 interact with matrix mostly elastically and the twin volume affected by slip relaxation is small as it is clearly illustrated in Figure 7.20. Therefore, the average stress values will not differ significantly for different precipitate thicknesses. The thick twin ($b/a = 0.2$) will cause plastic relaxation in larger area and also closer to the twin central region which is less influenced by the precipitates. Therefore the internal stress can be relaxed in the similar way regardless of the precipitate thickness. The case of 0.1 aspect ratio lies in between the previous scenarios.

The twin area affected by the slip relaxation is close enough to the twin tip to be affected by the precipitate thickness and also large enough to alter the average stress value.

The effect of precipitate on twin thickening process can be shown in Figure 7.16 where the absolute thickness of the precipitate is taken into account. The hindering effect of precipitate on twin thickening is increasing up to the certain value of twin thickness. When the twin aspect ratio reaches critical value, where it induces plasticity in larger area, the effect of the precipitate diminishes.

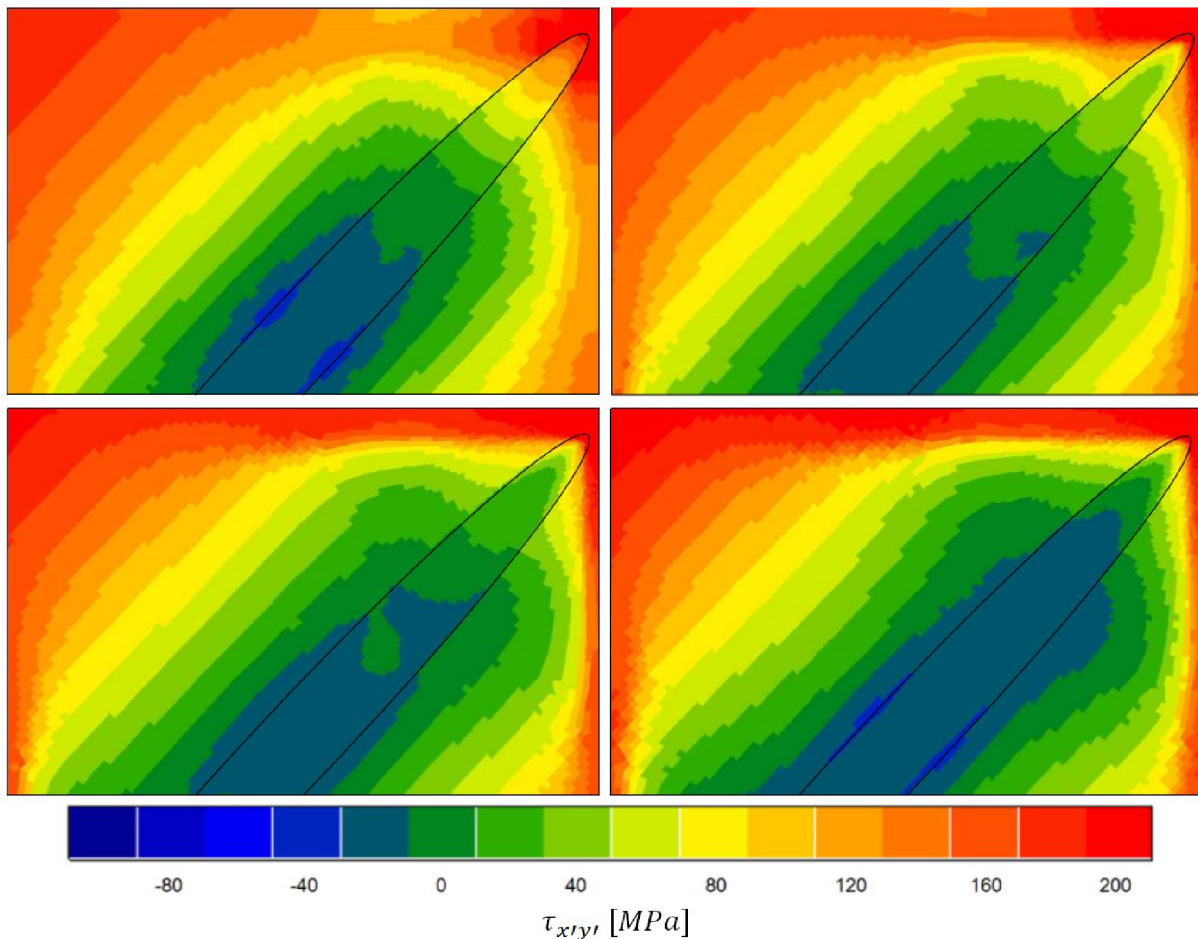


Figure 8.1 – Map of the $\tau_{x'y'}$ stress for 0.1 aspect ratio and different relative thickness of precipitates $\tau_R=175$ [MPa].

The shear stress field map of larger surroundings of the twin and precipitate is shown in Figure 8.2. It is the case for $b/a = 0.1$ and $\tau_R=175$ [MPa]. The map shows stress concentration inside the precipitate which is caused by its purely elastic behaviour. However the stress field „behind” the precipitate in the twin direction is not significantly influenced. Such observation suggests that conditions induced by the presence of the twin are not altered by the precipitate. Therefore the possibility of twin nucleation and propagation in this area is not significantly influenced. The stress level in the direction perpendicular to the twin axis is increasing with the precipitate thickness which can possibly help to accommodate twin with larger thickness next to the initial twin. Therefore the precipitates inhibits twin thickening but they can support nucleation and growth of multiple parallel twins.

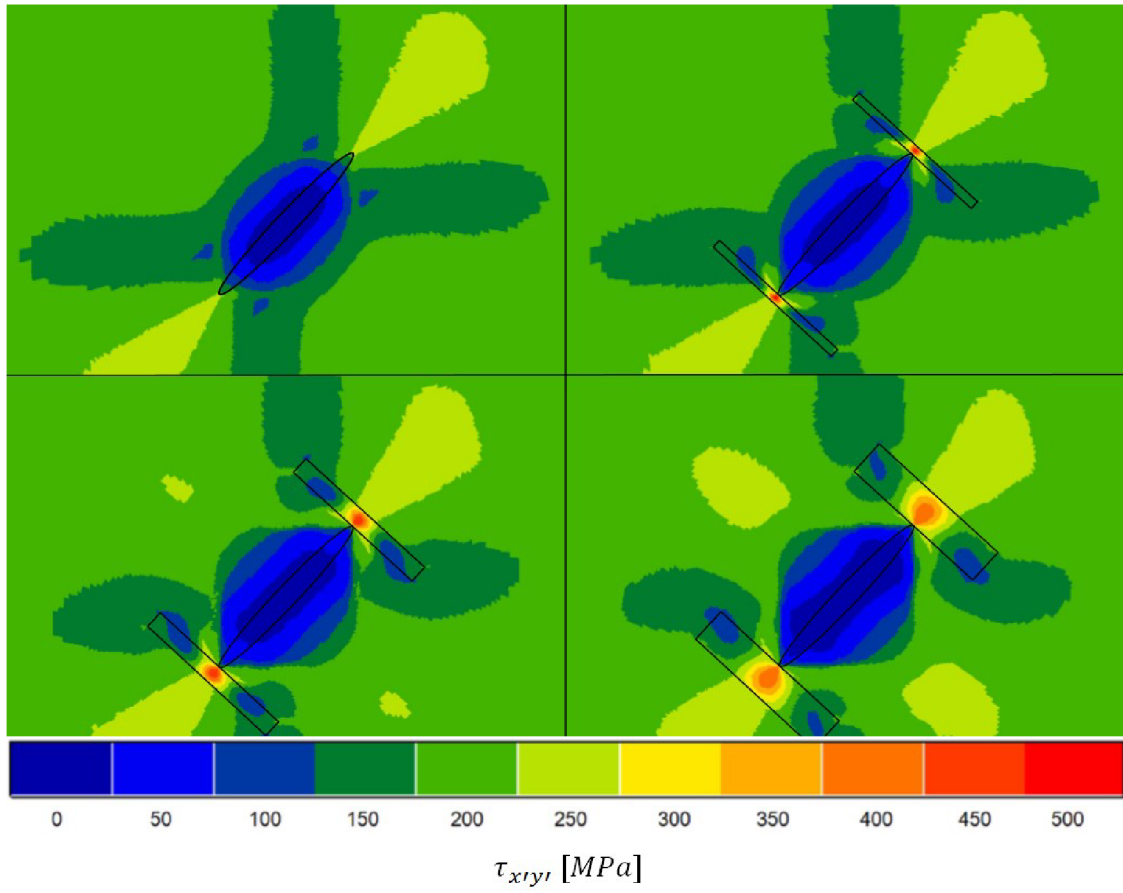


Figure 8.2 – Map of the τ_{xryr} stress for 0.1 aspect ratio and different relative thickness of precipitates $\tau_R=175$ [MPa].

9. Conclusions

The main goal of this thesis was to analyse the induced stress fields during the twinning, depending on the twin aspect ratio, size of the precipitates located at the tips of $\{1012\}\langle 10\bar{1}1\rangle$ tensile twins in AZ31 magnesium alloy via FEM crystal plasticity simulations. The results of the thesis can be summarized into the following points:

- Presence of precipitates increases the initial stress level needed for accommodation of twin with given aspect ratio. The stress level increases with increasing relative precipitate thickness.
- Precipitates influence mostly the stress level in the twin tip areas.
- The highest effect of precipitates was observed for aspect ratio 0.1 which suggests complex interaction between precipitate, twin and plastic zone around twin.
- Precipitates increase stress level in the side areas of the twin which can support nucleation and growth of multiple twins.

10. References

- [1] KAINER, U. K. *Magnesium alloys and technology*. Weinheim: DGM, 2003. ISBN 9783527605965.
- [2] *History of magnesium production*. [online]. [2017-05-25]. Retrieved from: <<http://www.magnesium.com/w3/data-bank/index.php?mgw=196>>
- [3] WULANDARI, W, BROOKS, G, RHAMDHANI, M and MONAGHAN, B. *Magnesium: current and alternative production routes*. [online]. 2010. Chemeca: Australasian Conference on Chemical Engineering. [2017-05-25]. Retrieved from: <<http://ro.uow.edu.au/cgi/viewcontent.cgi?article=2295&context=engpapers>>
- [4] CHRISTIAN, J. W., MAHAJAN, S. *Deformation twinning*. Progress in Materials Science. 1995, vol. 39. Pages 1-157
- [5] *Magnesium metal*. [online]. [2017-05-29]. Retrieved from: <<http://www.laxminarayansons.in/magnesium-metal.htm>>
- [6] PETERSEN, N. H., RIZLEY, J. H. *Magnesium processing*. [online]. [2017-05-25]. Retrieved from: <<https://www.britannica.com/technology/magnesium-processing3toc82154>>
- [7] Metalpedia. [online]. [2015-05-25]. Retrieved from: <<http://metalpedia.asianmetal.com/metal/magnesium/magnesium.shtml>>
- [8] *Magnesium alloys*. Engineering Casting Solutions. 2006. The American Foundry society. [online]. [2017-05-25]. Retrieved from: <<http://www.afsinc.org/files/images/magnes.pdf>>
- [9] SIOBHAN, F. *An Overview of Magnesium based Alloys for Aerospace and Automotive Applications*. Rensselaer Polytechnic Institute. 2012. [online]. [2017-05-25]. Retrieved from: <http://www.ewp.rpi.edu/hartford/~flemis2/EP/An_Overview_of_Magnesium_based_Alloys_for_Aerospace_and_Automotive_Applications.pdf>
- [10] *Magnesium and its alloys*. Suranaree University of Technology. 2007. [online]. [2017-05-25]. Retrieved from: <http://www.sut.ac.th/Engineering/metal/pdf/Nonferrous/03_Magnesium%20and%20magnesium%20alloys.pdf>
- [11] BETTLES, C. J., GIBSON, M. A. *Current Wrought Magnesium Alloys: Strengths and Weaknesses*. JOM. 2005. Pages 46-49
- [12] Magnesium Elektron datasheets. [online]. [2017-05-25]. Retrieved from: <<https://www.magnesium-elektron.com/datasheets/casting-alloys/>>

- [13] *Crystal Structures*. Academic resource center, Illinois Institute of Technology. [online]. [2017-05-25]. Retrieved from: <
[https://web.iit.edu/sites/web/files/departments/
academic-affairs/academic-resource-center/pdfs/Crystal_Structures.pdf](https://web.iit.edu/sites/web/files/departments/academic-affairs/academic-resource-center/pdfs/Crystal_Structures.pdf)>
- [14] HAZELL, P. J., APPLEBY-THOMAS, G. J., WIELEWSKI, E., ESCOBEDO, J. P. *The shock and spall response of three industrially important hexagonal close-packed metals: magnesium, titanium and zirconium*. Phil. Trans. R. Soc. 2014. <<http://dx.doi.org/10.1098/rsta.2013.0204>>
- [15] PARK, J. S., CHANG, Y. W. *The Effect of Alloying Elements on the c/a Ratio of Magnesium Binary Alloys*. Advanced Materials Research. Vols. 26-28. pages. 95-98. 2007
- [16] *Miller-Bravais indices for hexagonal close-packed crystals*. 2015. [online]. [2017-05-25]. Retrieved from: <<http://capitalenergy.biz/?p=25631>>
- [17] BUKHARI, M. U. *Crystal systems*. 2013. [online]. [2017-05-25]. Retrieved from: <<http://www.slideshare.net/umairbukhari3/crystal-systems>>
- [19] SADD, M. H., BUTTERWORTH-HEINEMANN, E. *Elasticity: Theory, Applications and Numerics*. 2005. ISBN 0-12-605811-3.
- [20] LUBLINER, J. *Plasticity theory*, 2006, revised edition (PDF)
- [21] *Deformation twinning*. [online]. [2017-05-25]. Retrieved from <[https://www.doitpoms.
ac.uk/tlplib/superelasticity/twinning.php](https://www.doitpoms.ac.uk/tlplib/superelasticity/twinning.php)>
- [22] *Linear Defects*. NDT Resource Center. [online]. [2017-05-25]. Retrieved from <[https://www.nde-ed.org/EducationResources/CommunityCollege/
Materials/Structure/linear_defects.htm](https://www.nde-ed.org/EducationResources/CommunityCollege/Materials/Structure/linear_defects.htm)>
- [23] *Imperfections in Solids*. 2017. [online]. [2017-05-25]. Retrieved from: <[http://www.slid
eserve.com/shawna/chapter-5-imperfections-in-solids](http://www.slideserve.com/shawna/chapter-5-imperfections-in-solids)>
- [24] LINDEKE. *Crystal Defects and Noncrystalline Structure-Imperfection*. [online]. [2017-05-25]. Retrieved from: <<http://slideplayer.com/slide/5014115/>>
- [25] KAILAS, S. V. *Dislocations and Strengthening Mechanisms*. Indian Institute of Science. [online]. [2017-05-25]. Retrieved from <[http://nptel.ac.in/courses/
112108150/pdf/Lecture_Notes/MLN_06.pdf](http://nptel.ac.in/courses/112108150/pdf/Lecture_Notes/MLN_06.pdf)>

- [26] LUQUE, A., GHAZISAEIDI, M., CURTIN, W. A. *Deformation modes in magnesium (0001) and (01-11) single crystals: simulations versus experiments*. Modelling Simul. Mater. Sci. Eng. 2013. DOI:10.1088/0965-0393/21/4/045010
- [27] SISKI, F., STRATIL, L., CIZEK, J., GHADERI, A., BARNETT, M. *Numerical analysis of twin thickening process in magnesium alloys*, Acta Materialia, Volume 124, 2017, Pages 9-16
- [28] GHARGHOURI, M. A., WEATHERLY, G. C., EMBURY, J. D. *The interaction of twins and precipitates in a Mg-7.7 at.% Al alloy*, Philosophical Magazine A, 1998, Pages 1137-1149, DOI: 10.1080/01418619808239980
- [29] *The Finite Element Method*. [online]. [2017-05-25]. Retrieved from: <<https://www.comsol.com/multiphysics/finite-element-method>>
- [30] BURSA, J. Materials for the applied mechanics course [online]. [2017-05-23]. Retrieved from: <<http://www.umt.fme.vutbr.cz/~jbursa/>>
- [31] ROBSON, J. D. *The effect of internal stresses due to precipitates on twin growth in magnesium*, Acta Materialia, Volume 121, December 2016, Pages 277-287, ISSN 1359-6454
- [32] Solid State Phenomena, Volume 191, 2012, Pages 151-158, Trans Tech Publications, Switzerland, DOI: 10.4028/www.scientific.net/SSP.191.151
- [33] ESHELBY, J. D. *The Determination of the Elastic Field of an Ellipsoidal Inclusion, and Related Problems*. Proc. R. Soc. Lond. A 1957, pages 376-396, DOI: 10.1098/rspa.1957.0133
- [34] SISKI, F. *Continuum vs. Dislocation dynamics modelling of thin films*. Thesis. L'Ecole des Mines de Paris. 2007

11. Used symbols and variables

$CRSS$		Critical resolved shear stress
FEM		Finite element method
b	[hkl]	Burgers vector
u_i	[m]	Displacement
γ^p	[-]	Plastic shear strain
$\dot{\gamma}^p$	[s ⁻¹]	Plastic shear strain rate
ρ	[m ⁻²]	Density of dislocations
ρ_m	[m ⁻²]	Density of mobile dislocations
\bar{v}	[m.s ⁻¹]	Average dislocation velocity
τ	[MPa]	Shear stress
W	[J]	Strain energy
α	[-]	Numerical factor
G	[MPa]	Shear modulus
σ_y	[MPa]	Yield stress
τ^S, τ_r, σ_i	[MPa]	Critical resolved shear stress
K_y	[-]	Unpinning constant
D	[m]	Grain diameter
c/a	[-]	Aspect ratio
g	[-]	Shear strain
X_i	[-]	Coordinate associated to undeformed geometry
x_i	[-]	Coordinate associated to deformed geometry
ε_{ij}	[-]	Engineering strain
G_i	[N]	Volumetric force
σ_{ij}	[MPa]	Cauchy stress tensor

C_{ijkl}	[-]	Stiffness tensor
Π	[J]	Elastic potential energy
P	[J]	Potential energy associated to loads
o	[N]	Volumetric force
p	[N]	Surface force
N_i	[-]	Basis function
$u(x, y, z)$	[-]	Approximate displacement function
a	[length unit]	Twin length
b	[length unit]	Twin thickness
t_p	[length unit]	Precipitate thickness
F	[-]	Deformation gradient tensor
λ_{ij}	[-]	Stretch
m^s	[hkil]	Slip direction
n^s	[hkil]	Normal to the slip plane
K, n	[-, -]	Norton law parameters
x^s, r^s	[-, -]	Isotropic and kinematic hardening variable
q, b	[MPa, -]	Crystal plasticity material model parameters
E	[MPa]	Young's modulus
μ	[-]	Poissons ratio
h^{sr}	[-]	Hardening matrix